

This is an Accepted Manuscript for *Journal of Glaciology*. Subject to change during the editing and production process.

DOI: 10.1017/jog.2026.7:

1 Progression of the surge in the Negribreen Glacier System 2 from two years of ICESat-2 measurements

3 Thomas TRANTOW,¹ Ute C. HERZFELD,¹

4 ¹*Department of Electrical, Energy and Computer Engineering, University of Colorado, Boulder,*
5 *Colorado, USA*

6 *Correspondence: Thomas Trantow <trantow@colorado.edu>*

7 **ABSTRACT.** The state-of-the-art measurement capabilities of ICESat-2 allow
8 high spatiotemporal resolution of complex ice-dynamic processes that occur
9 during a surge. Detailed and precise mapping of height changes on surge
10 glaciers has previously escaped observations from space due to the limited
11 resolution of space-borne altimeter data and the surface characteristics of
12 glaciers during surge, such as heavy crevassing. This makes geophysical
13 interpretation of deformation and assessment of mass transfer difficult. In
14 this paper, we present an approach that facilitates analysis of the evolution
15 of geophysical processes during a surge, including height changes, crevassing,
16 mass transfer and roughness. We utilize all data from 2 years of ICESat-
17 2 observations collected during the mature phase of the Negribreen Glacier
18 System surge in 2019 and 2020. The progression of Negribreen's surge has
19 resulted in large-scale elevation changes and wide-spread crevassing, making it
20 an ideal case study to demonstrate ICESat-2 measurement capabilities, which
21 are maximized when coupled with the Density Dimension Algorithm for ice
22 surfaces (DDA-ice). Results show expansion of the surge in upper Negribreen
23 which demonstrates the ability of ICESat-2/DDA-ice to measure a rapidly
24 changing surge glacier and provide the best estimates for cryospheric changes
25 and their contributions to sea-level rise.

This is an Open Access article, distributed under the terms of the Creative Commons Attribution-NonCommercial-NoDerivatives licence (<http://creativecommons.org/licenses/by-nc-nd/4.0/>), which permits non-commercial re-use, distribution, and reproduction in any medium, provided the original work is unaltered and is properly cited. The written permission of Cambridge University Press must be obtained for commercial re-use or in order to create a derivative work.

26 1. INTRODUCTION

27 1.1. Glacier Surging: Relevance, Complexity and Observation from Space

28 Processes of ice-dynamic instability, such as glacial acceleration, have been identified by the
29 Intergovernmental Panel of Climate Change (IPCC, AR6, Chen and others (2021)) as a source of “deep
30 uncertainty” in our understanding of ice sheet and glacier evolution and their contribution to future sea-
31 level rise. Glacier surging is a type of glacial acceleration (Clarke, 1987; Truffer and Echelmeyer, 2003),
32 and is incompletely understood because surges are relatively rare events with dramatic ice deformation
33 that occurs on short timescales, which results in a paucity of comprehensive observations relative to other
34 acceleration types. While more extensive surge observations have been conducted with the advance of
35 satellite technology (e.g., Dunse and others (2015); Trantow and Herzfeld (2016); Goerlich and others
36 (2020); Paul and others (2021); Kääb and others (2023); Trantow and Herzfeld (2024)), few of these are of
37 a resolution to detect surface-structure signatures of dynamic change, especially with respect to crevassing,
38 and none so far have used ICESat-2. Here we employ the unique capabilities of ICESat-2 to retrieve surface
39 heights of crevassed ice with the detail needed to infer dynamic and kinematic information of a surging
40 glacier from morphological cross sections.

41 A surge-type glacier will cycle quasi-periodically between a long quiescent phase of normal flow and a
42 short surge phase when flow speeds rapidly accelerate by a factor of 10 to 200. Negribreen, a large glacier in
43 eastern Spitsbergen, Svalbard, began to surge in 2016 for the first time in over 80 years (Lefauconnier and
44 Hagen, 1991; Strozzi and others, 2017; Herzfeld and others, 2021). Negribreen continues to surge through
45 2023, though it is gradually decelerating from its peak velocities in 2017 (Haga and others, 2020; Herzfeld
46 and others, 2022). A feed-back system of acceleration, crevassing and ice-ocean interaction has already led
47 to accelerated mass loss of the Negribreen Glacier System. There is a possibility that the Negribreen surge
48 may trigger pervasive mass loss and a potential disintegration of the entire glacier system, similar to the
49 collapse of the Vavilov Ice Cap in the Russian Arctic (Willis and others, 2018).

50 Surges are limited geographically to particular regions of the cryosphere, clustered mostly in
51 Alaska/Yukon, Svalbard, high mountain Asia and around the periphery of the major ice sheets (Dolgushin
52 and Osipova, 1975; Kamb and others, 1985; Herzfeld and Mayer, 1997; Björnsson and others, 2003; Jiskoot
53 and others, 2003; Jiskoot, 2011; Flowers and others, 2011; Sevestre and others, 2015; Bhambri and others,
54 2017; Trantow and Herzfeld, 2018; Kochtitzky and others, 2020; Vale and others, 2021; Banerjee and
55 others, 2022; Yao and others, 2023; Guillet and others, 2022). While new satellite technologies have allowed

56 detection of over 100 surge-type events from 2017-2022 (Kääb and others, 2023), very few of these events
57 have received dedicated studies that map and document individual surges, making investigation of surge
58 mechanisms and processes a data-starved problem.

59 Geophysical processes that are characteristic of a surge include rapid acceleration, crevassing, mass
60 transfer within the glacier, advance of the ice front, and changes in the internal hydrological system
61 of the glacier (Meier and Post, 1969; Kamb, 1987; Harrison and Post, 2003; Truffer and others, 2021).
62 Altimetry is capable of measuring these first four surge characteristics in particular. However, observations
63 of surge glaciers from space typically use radar or optical imagery (e.g., Guan and others (2022); Wuite
64 and others (2022); Kääb and others (2023); Liu and others (2024); Main and others (2024)), which usually
65 focus on velocity or elevation-change analysis yet lack the spatial resolution to resolve crevasses, and field
66 measurements (e.g., Kamb and others (1985); Björnsson and others (2003); Herzfeld and others (2013b);
67 Lovell and Fleming (2023); Herzfeld and others (2022)), which are relatively rare and often lack spatial
68 and/or temporal coverage.

69 High resolution optical imagery from Maxar's Worldview satellites has allowed surge analysis at the
70 meter to submeter resolution (Herzfeld and others, 2024; Liu and others, 2024) in the horizontal direction.
71 However, heavy crevassing of the ice surface characteristic during a surge can complicate elevation analysis
72 at high resolution resulting in more coarse analysis in the vicinity of crevasse fields (e.g., 250 m resolution
73 in crevassed areas in Liu and others (2024)).

74 In this paper, we present an approach that facilitates high-resolution (1-5 m) analysis of the evolution of
75 geophysical processes during a surge, including height changes, crevassing, mass transfer in the glacier and
76 roughness. We utilize all data from 2 years of ICESat-2 observations collected during the mature phase of
77 the Negribreen surge in 2019 and 2020. The measurement capabilities of ICESat-2 allows resolution of the
78 complex ice-dynamic processes that occur during a surge in space and time in an altimeter data set.

79 **1.2. The Study Area: Negribreen, Svalbard**

80 The Negribreen Glacier System, located in eastern Svalbard (Fig. 1), surged in late 2016 reaching speeds
81 of 21m/day during its peak in July 2017, equivalent to 200 times its normal quiescent velocity (Strozzi
82 and others, 2017; Herzfeld and others, 2021). In response to this rare event, the authors' Geomathematics,
83 Remote Sensing and Cryospheric Sciences Group at the University of Colorado, Boulder, conducted three
84 airborne survey campaigns of the glacier system in the summers of 2017, 2018 and 2019 (Herzfeld and
85 others, 2022), whose data supplement the analysis in this paper (see Section 2.2).

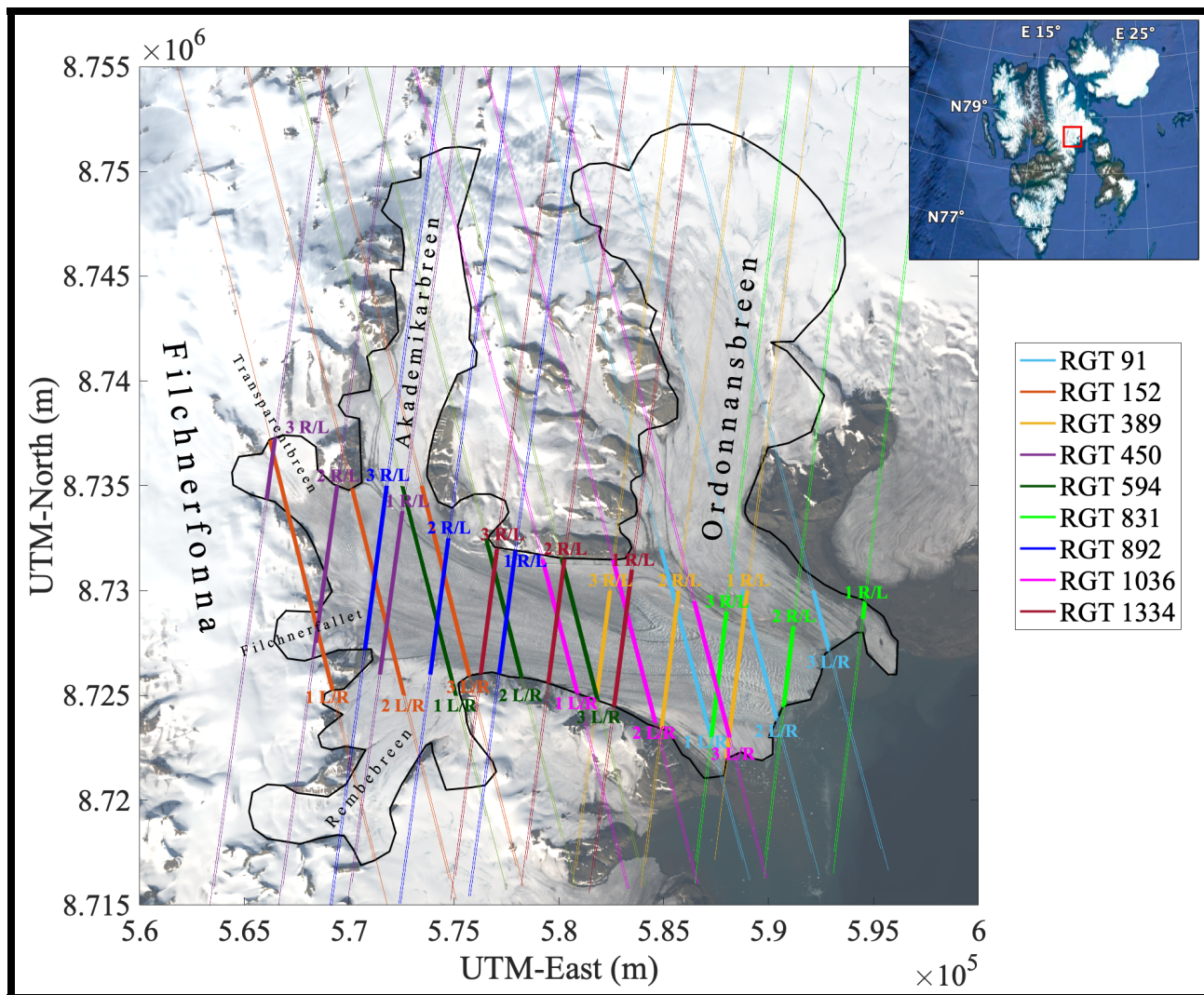


Fig. 1. ICESat-2 survey lines over the Negribreen Glacier System. The survey lines for each of ICESat-2's three beam-pairs are color coded by their Reference Ground Track (RGT) while the Negribreen Glacier System borders are given by the black line. The thick lines correspond to the part of the track that is analyzed in this paper which is mostly equivalent to the boundaries of Negribreen Glacier. Left/Right (L/R) beam-pairs are separated by ~ 90 m on-ice which is within line thickness over Negribreen in this figure. The insert in the upper right gives the location of the Negribreen Glacier System (red box) within the Svalbard archipelago. Background image from Landsat-8 acquired 5 August 2019.

86 The Negribreen Glacier System consists of Negribreen, where the majority of the surge activity occurs,
 87 Rembebreen, a southern tributary glacier in the upper glacier system, and two main tributary glaciers
 88 flowing in from the north: Akademikarbreen that feeds Negribreen in the upper glacier, and Ordonnansbreen
 89 further downglacier (Fig. 1). The Negribreen Glacier System receives large amounts of inflowing ice from
 90 the Filchnerfonna accumulation zone above the Negribreen Glacier System to the west. The divide between

91 Filchnerfonna and the Negribreen Glacier System as we have defined it in this paper is somewhat arbitrary
92 as the two ice masses are connected by a series of glaciers and ice falls (e.g., Transparentbreen and
93 Filchnerfallet) and are dynamically connected, which we show in this paper. However, the vast majority
94 of the surge activity, particularly in 2019 and 2020, occurs below the Filchnerfonna and as such we define
95 the bounds of the Negribreen Glacier System using the black line in Fig. 1, which excludes Filchnerfonna.

96 Negribreen consists of polythermal ice and is marine-terminating and thus the mechanisms leading to
97 surge behavior, along with surge evolution as a whole, differ from those of a surge in a temperate and/or
98 land-terminating glacier such Bering Glacier, Alaska (Dowdeswell and others, 1984; Murray and others,
99 2003; Trantow, 2020), though some unifying surge theories have been postulated (e.g., Benn and others
100 (2019)). Similar to other observed surges in tidewater glaciers in Svalbard (Strozzi and others, 2017; Nuth
101 and others, 2019), Negribreen began accelerating near the terminus after a collapse in the frontal area
102 (location indicated in Fig. 2a), and surge effects, such as crevassing and increased velocities, propagated
103 upglacier affecting other parts of the greater Negribreen Glacier System (Herzfeld and others, 2021; Haga
104 and others, 2020). High velocities and enhanced calving occurring during the surge led to extensive mass
105 loss in the system, which has contributed to sea-level rise.

106 The mass loss and disintegration of the glacier system is immediately apparent by examining the time
107 series of Landsat-8 imagery in Fig. 2 from 2018-2021 (RGB imagery at 30 m resolution, Roy and others
108 (2014)). The Negribreen Glacier System terminus has seen massive deformation with the “tooth” of
109 Ordonnansbreen becoming completely detached from the main system by 2021 (see Fig. 2d). Detailed
110 altimeter documentation of the Ordonnansbreen tooth detachment is provided by the ICESat-2/DDA-ice
111 time series in Section 4.3.3.

112 1.3. ICESat-2 and the DDA-ice

113 NASA’s ICESat-2 satellite, launched on 15 September 2018, provides high-resolution height measurements
114 of ice sheets and glaciers via its state-of-the-art micro-pulse photon-counting lidar technology (Markus and
115 others, 2017; Neumann and others, 2019). ICESat-2’s payload, the Advanced Topographic Laser Altimeter
116 System (ATLAS), provides height observations at a nominal 0.7 m along-track resolution (under clear-
117 sky atmospheric conditions), a significant upgrade to its predecessor, ICESat’s Geoscience Laser Altimeter
118 System (GLAS), which provided height estimates every 173 m along-track from 2003-2009 (also constrained
119 by atmospheric conditions) (Zwally and others, 2002).

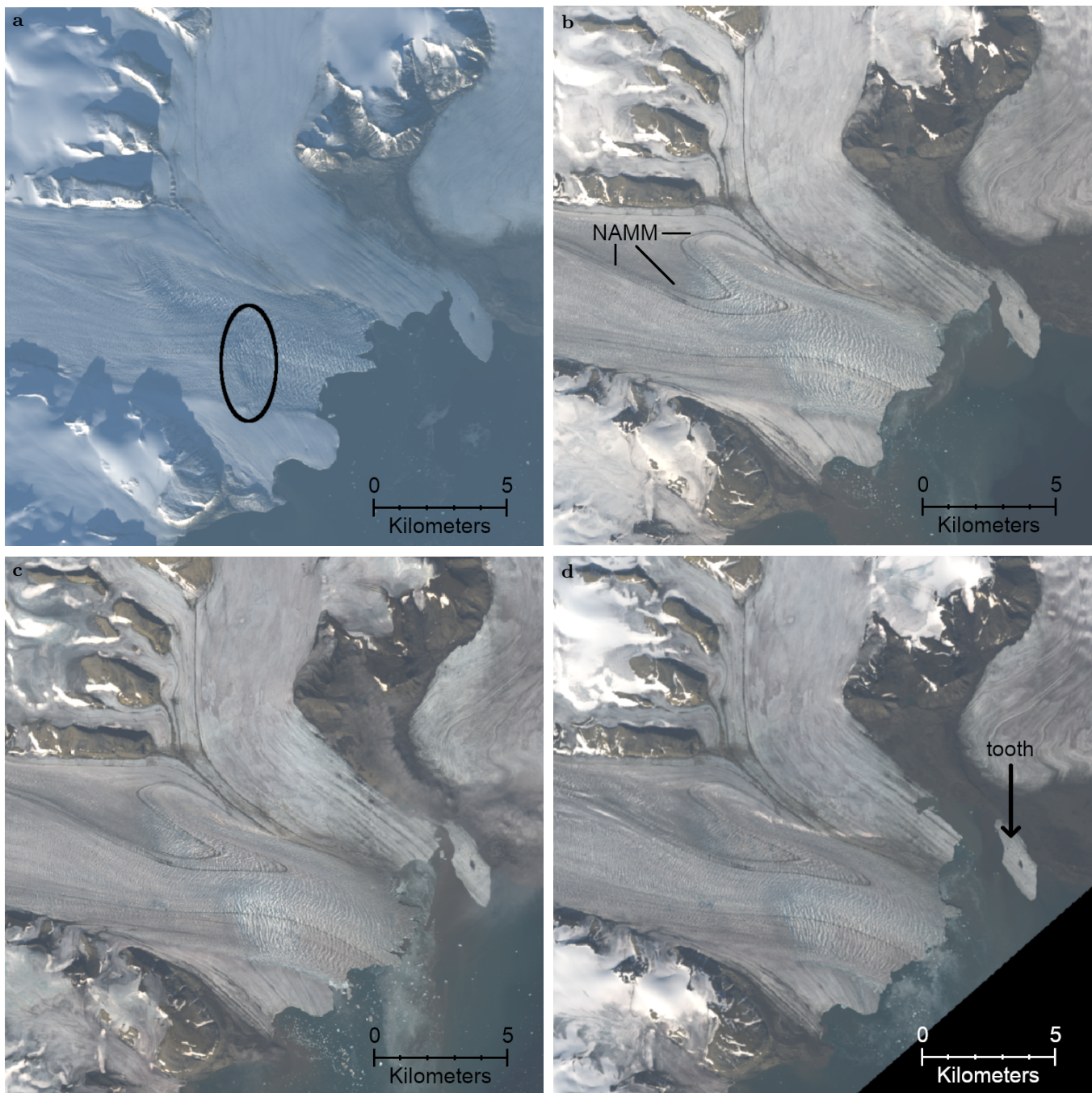


Fig. 2. Landsat-8 images of the Negribreen Glacier System 2018-2021. Landsat-8 RGB imagery (30 m resolution) acquired (a) 30 September 2018 with the location of the surface collapse that initiated the surge circled in black, (b) 20 August 2019 with black lines indicating the lower part of the Negribreen-Akademikarbreen Medial Moraine (NAMM) which has “folded” due to the surge, (c) 31 July 2020 and (d) 8 August 2021 with Ordonnansbreen’s tooth indicated by the black arrow.

120 ATLAS operates at a wavelength of 532 nm (green light) and consists of 3 pairs of strong and weak beams
 121 with each pair separated by 3.3 km in the across-track direction (Neumann and others, 2019; Martino and
 122 others, 2019). Each strong beam is separated from its weak counterpart by 90 m across-track and 2.5 km

123 along-track. The ratio of transmit energies between strong and weak is approximately 4:1. The transmitter
124 array is rotated approximately every 6-months so that either the weak beams lead (flying “forwards”,
125 spacecraft orientation = 1), or the strong beams lead (flying “backwards”, spacecraft orientation = 0)(see
126 Fig. 3 and Table 1 of Herzfeld and others (2021)).

127 ICESat-2 flies at ~ 500 km altitude and orbits in a 92° inclination, and thus provides measurements up
128 to $\pm 88^\circ$ latitude. The satellite orbits in an exact 91-day repeat cycle with 1387 reference ground tracks
129 (RGTs) (Neumann and others, 2019, 2020b). All-in-all, ICESat-2 provides 6 measurement opportunities
130 across a 6.6 km swath every 0.7 m along its flight path, repeating every 91 days.

131 Several factors limit the ideal spatiotemporal measurement resolution of ICESat-2 in the cryosphere,
132 the most significant being cloud cover which severely attenuates green light. Other factors contributing
133 to weak or non-existent return signals over ice include diffuse scattering, the presence of water or dirt,
134 and pre-scheduled satellite maneuvers that either pause active measurement for maintenance or calibration
135 purposes, or point the instrument off its normal track in order to better capture a particular phenomenon
136 (Luthcke and others, 2021; Magruder and others, 2021). Signals are further complicated by noise emanating
137 from the solar background or from the instrument itself (Martino and others, 2019). Furthermore, NASA’s
138 official ice-surface height product ATL06 (Smith and others, 2020) only resolves surface heights with 40 m
139 postings at 20 m spacing and does not take full advantage of the high-resolution capabilities of ICESat-2
140 (Herzfeld and others, 2021).

141 The Density-Dimension Algorithm for ice surfaces (DDA-ice), however, fully exploits ICESat-2’s
142 measurement capabilities by identifying height-signals at the sensor resolution of 70 cm (Herzfeld and
143 others, 2017, 2021). At this resolution, important geophysical processes can be measured such as crevassing,
144 calving and rifting (Herzfeld and others, 2021). In the present study, we employ the DDA-ice in order to
145 maximize ICESat-2’s ability to capture geophysical processes in a rapidly changing glacier system that is
146 actively surging.

147 **2. DATA**

148 **2.1. ICESat-2 ATL03 Data**

149 The DDA-ice algorithm takes as input the ATLAS/ICESat-2 L2A Global Geolocated Photon Data (ATL03)
150 (Neumann and others, 2020b). We use release 4 (revision 1) of these data in this analysis (Neumann and

151 others, 2020a). The ATL03 data give height above the WGS 84 ellipsoid (ITRF2014 reference frame) along
152 with latitude, longitude and time for all the photons downlinked from ICESat-2.

153 ATL03 data are segmented by granules that each cover 1/14th of a single orbit. Granules are given
154 in HDF5 format and are freely available through NASA or from the National Snow and Ice Data
155 Center (NSIDC). Granules are named using the format ATL03-[yyyymmdd][hhmmss]-[tttccss]-[vvv_rr].h5,
156 where[yyyymmdd][hhmmss] is the date and time of acquisition associated with the first data point in the
157 granule, [tttt] is the reference ground track (RGT) number, [cc] the cycle number, [ss] the segment number
158 and [vvv_rr] the version and revision numbers.

159 For our analysis, we attain all granules covering the Negribreen Glacier System between 1 January 2019
160 and 31 December 2020. With the Negribreen Glacier System lying between latitudes 78.5°N 78.8°N, the
161 segment number is equal to either 03 if the satellite is ascending during data collection or equal to 05
162 if the satellite is descending. The cycle number identifies the number of 91-day cycles that have elapsed
163 since ICESat-2 entered its science orbit. Our analysis here uses data that spans eight cycles from cycle 02
164 to cycle 09. Each cycle is divided into 1387 unique Reference Ground Tracks (RGTs). There are 9 RGTs
165 that provide significant data coverage of the Negribreen Glacier System: 91, 152, 389, 450, 594, 831, 892,
166 1036 and 1334. Nine RGTs spanning 8 cycles equates to 72 granules for this two-year analysis. With all
167 six beams covering part of the glacier system for each RGT, we process a total of 432 measurement passes
168 in this analysis. The specific granules used in this analysis are identified in the Supplementary Material
169 (negri_data_2019_2020.xlsx).

170 ICESat-2's six beams are labeled as gt1l, gt2l, gt3l, gt1r, gt2r and gt3r. The strong beams can be
171 associated with either the left (l) or right (r) side depending on the orientation of the ICESat-2 observatory,
172 which switches every six months or so in order to maximize the solar illumination of the solar panels. At
173 the beginning of 2019, ATLAS was in its "backward" orientation with left ground tracks corresponding
174 to strong beams and right ground tracks corresponding to weak beams. ATLAS switched to its "forward"
175 orientation in September 2019 resulting in strong beam identification by the right ground tracks. A switch
176 back to the "backwards" orientation occurred in June 2020.

177 **2.2. Airborne Altimeter and Image Data**

178 The authors, along with other members of the Geomathematics, Remote Sensing and Cryospheric Sciences
179 research group, collected airborne imagery and altimeter data in the summers of 2017, 2018 and 2019
180 as part of a campaign to document the surge of Negribreen (Herzfeld and others, 2022; Herzfeld and

181 Trantow, 2021). Each field campaign gives a synoptic view of the entire glacier at a single point in time,
182 providing a tie-in for satellite data, e.g. ICESat-2 tracks, which are spaced out. The analysis in the current
183 paper utilizes the imagery collected during the 2019 campaign, which under-flew several ICESat-2 tracks in
184 upper Negribreen on 13 August 2019. Airborne altimetry data are used to validate the crevasse spacing and
185 crevasse depth, as shown in Herzfeld and others (2021) and Herzfeld and others (2022), and complement
186 our findings presented later in the paper. Here, we give a quick summary of the 2019 Negribreen campaign
187 and the instruments that were employed to document the surge.

188 For the 2019 campaign, height measurements were attained using a LaserTech Universal Laser System
189 (ULS) instrument that operates at 905 nm. The ULS was used in conjunction with a 1-Hz LORD 3DM-
190 GX5-15 Virtual Reference Unit, i.e. an IMU, along with a 10-Hz Trimble R10 rover GPS in order to attain
191 accurate height estimates. Both the ULS and GPS were attached to the skids of a helicopter which was
192 flown 100-200 m above the ice surface during operation of the laser. With an effective measurement rate
193 of 400 Hz, the ULS provided glacier surface heights every 0.06-0.08 m along-track.

194 Specifically, the 2019 flight campaign under-flew two beam pairs: RGT 594 (gt1l and gt1r) from 5 August
195 2019, and RGT 450 (gt1l and gt1r) from 18 August 2019 (Herzfeld and others, 2022). These two tracks
196 passed over interesting crevassed areas in upper Negribreen (Fig. 1) and their dates of collection coincided
197 with the field campaign. Crevasse characteristics along these tracks were quantified in Herzfeld and others
198 (2021) and Herzfeld and others (2022) which found a close agreement between crevasse morphology, spacing
199 and depth between ULS data and ICESat-2 data.

200 Selected photos from the 2019 campaign, taken with a handheld Nikon D5100 Single-Lens Reflex camera,
201 are given in Fig. 3. During the campaign in August 2019, much of the lower glacier was covered in low-lying
202 mixed-phase clouds (Shupe and others, 2011; Gierens and others, 2020) (Fig. 3a). Mixed-phase clouds in
203 Svalbard occur in every season within 1 km of the surface, and have a complicated structure consisting of
204 supercooled liquid and ice layers that obviously obscure the glacier ice-surface (Gierens and others, 2020).
205 These ephemeral low-lying clouds restricted airborne surveys to the upper Negribreen Glacier System for
206 several, but not all, flights in 2018 and 2019.



Fig. 3. Imagery from the airborne campaign flights over Negribreen in August 2019. (a) Low-lying clouds covering the lower glacier and terminus (photo looking downglacier). (b) Young surge crevasses in upper Negribreen. (c) Large and complex crevasses exceeding 30 m depth in the center-front of the glacier just above the terminus. (d) Snow-bridged crevasses seen most clearly in the left-foreground with the white, fresh snow covers the top of the open crevasses. (e) Water-filled crevasses. (f) Crevasses near the Negribreen-Akademikarbreen Medial Moraine (NAMM) are filled with water indicating a disruption in the local englacial drainage system. Fresh crevassing through surge expansion affected this area along the northern NAMM in early 2020, shortly after this photo was taken.

207 **2.3. Sentinel-1 SAR Data**

208 We used Synthetic Aperture Radar (SAR) imagery from the European Space Agency's (ESA's) Sentinel-1
209 satellite (Geudtner and others, 2014) to derive velocity estimates on Negribreen. Mean velocity estimates
210 are derived for several characteristic time periods between 2019 and 2020 which are used to supplement
211 the ICESat-2 analysis by providing basic information on changes in the velocity field associated with the
212 surge.

213 There are two Sentinel-1 satellites labeled A and B, which in tandem provide repeat imagery every six
214 days for a given location. ESA freely provides the Sentinel Application Platform (SNAP) software to derive
215 surface velocity estimates for ice sheets and glaciers using offset tracking methods (Veci and others, 2014).
216 Offset tracking methods measure feature motion between two images using patch intensity cross-correlation
217 optimization.

218 Over Negribreen, Sentinel-1 operates in the Interferometric Wide (IW) swath mode acquiring data with
219 a 250 km swath at 5 m by 20 m spatial resolution. The SNAP toolbox offset tracking method takes as
220 input the Level-1 Ground Range Detected (GRD) product from two Sentinel-1 images. These images are
221 separated by a temporal baseline, which in our analysis is usually equal to 12-days, i.e. the length the
222 repeat cycle of a single Sentinel-1 satellite. The GRD products are updated with more accurate orbit
223 data and are then coregistered based on geometry given by the ACE-30 Digital Elevation Model (DEM).
224 We then perform offset tracking providing a 300 m by 300 m resolution velocity product with missing or
225 low-confidence data interpolated up to 1 km. A velocity estimate is considered low-confidence if its cross-
226 correlation value falls below a threshold of 0.1 as determined by the SNAP offset tracking software (Veci
227 and others, 2014).

228 Four characteristic velocity maps from 2019 to 2020 are provided in Fig. 4 (see `negri_data_2019_2020.xlsx`
229 for specific Sentinel-1 data products used). It is clear in each map that Negribreen is surging, reflected by
230 elevated speeds (> 1 m/day), while the tributary glaciers remain at typical quiescent speeds well below 1
231 m/day. Velocity magnitudes are largest near the front of Negribreen and decrease across its length with
232 elevated speeds still present near the border with Filchnerfonna in the upper glacier.

233 Fig. 4a displays mean velocity magnitudes near the beginning of our study period between 4 February
234 2019 and 16 February 2019, with maximal velocities reaching 9 m/day. Mean velocity magnitudes for
235 Negribreen remain at this level throughout the winter months of early 2019 and do not begin to decrease
236 until August of 2019.

237 Fig. 4b provides mean velocity estimates between 11 August 2019 to 23 August 2019, corresponding to
238 the time of the August 2019 field campaign of (Herzfeld and others, 2022). Maximal surge speeds were
239 near 6 m/day. As Negribreen transitions into its mature surge phase by 2019, the seasonal component of
240 velocity becomes more apparent as reflected by a significant slowdown in August from maximums typically
241 occurring in July.

242 Fig. 4c provides mean velocities between 10 July 2020 and 22 July 2020 when the glacier system is
243 moving its fastest for the year due to an abundance of meltwater that lubricates the glacier base. Maximal
244 velocities in July 2020 reached 10 m/day, similar to those in July 2019.

245 Finally, Fig. 4d gives mean velocities between 19 December 2020 and 31 December 2020 near the end
246 of our analysis period. This map provides typical velocities during winter time in Negribreen in 2020 with
247 maximal velocities around 4 m/day.

248 3. METHODS

249 3.1. DDA-ice: High Resolution Surface Heights from ICESat-2 Data

250 We applied the DDA-ice algorithm to the raw photon data found in ATL03 to identify the ice-surface signal
251 at sensor resolution, which is then interpolated at 5 m resolution for smooth ice and 1 m resolution for
252 rough ice to attain a final ice-surface height estimate that is used for further analysis. The full mathematical
253 description of the DDA-ice is found in Herzfeld and others (2017) and Herzfeld and others (2021).

254 The central idea of the DDA-ice is to calculate the density-field for the returned photon point cloud
255 using a convolution defined by a density operator (Herzfeld and others, 2017). Density is then used for
256 classification of signal photons versus background photons in the photon cloud. The density operator,
257 applied to each photon, employs a radial basis function that weights neighboring photons with a 2D
258 anisotropic Gaussian kernel. Signal-noise separation utilizes an auto-adaptive threshold function, i.e., a
259 function that automatically adapts to highly variable photon density characteristics including apparent
260 surface reflectance, different background characteristics based on the time of day and some instrument-
261 related artifacts. In addition to identification of surface height in signal photons, the DDA-ice provides
262 interpolated surface heights using a function termed “ground follower” for short. The ground follower
263 employs a piece-wise linear function that is weighted by density values associated with signal photons
264 in the segment of the interpolator. Segment length depends on surface roughness, calculated from signal
265 photons.

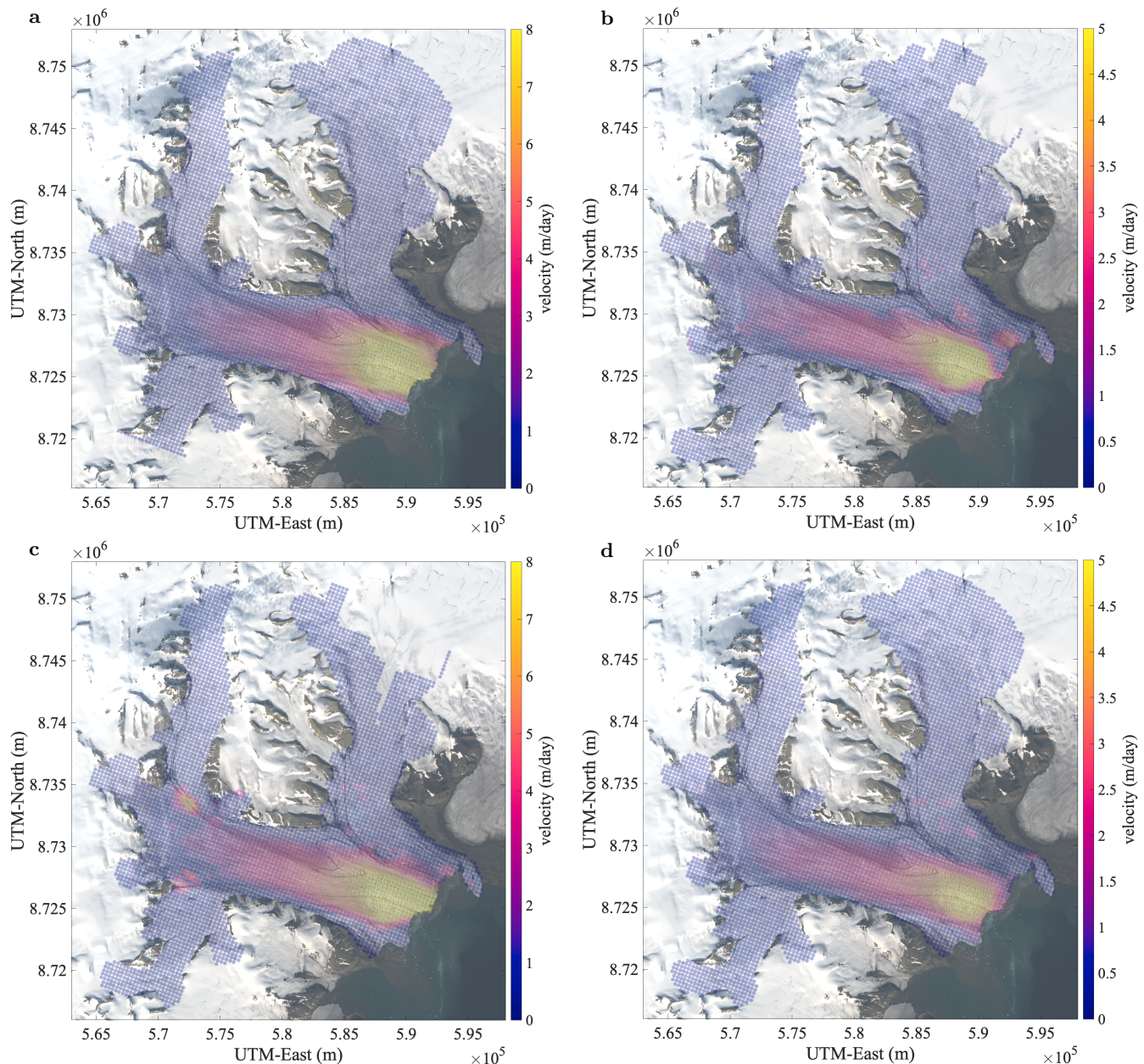


Fig. 4. Negribreen velocity maps from 2019-2020. Maps derived from Sentinel-1 SAR data. (a) Mean surface velocities between 4 February 2019 and 16 February 2019 (m/day). (b) Mean surface velocities between 11 August 2019 and 23 August 2019 (m/day). This baseline spans the 2019 airborne campaigns in August 2019. (c) Mean surface velocities between 10 July 2020 and 22 July 2020 (m/day) with maximum speeds exceeding 8 m/day. (d) Mean surface velocities between 19 December 2020 and 31 December 2020 (m/day) at the end of the study period in December 2020 which shows typical velocities during the winter months of 2020. Only velocity estimates with a cross-correlation ratio above 0.1 are displayed (Veci and others, 2014).

266 The DDA-ice uses algorithm-specific parameters to best identify the type of surface under investigation.
 267 Three important parameters that control the shape of the weighting kernel include the standard deviation
 268 of the Gaussian distribution (σ , s), the amount of standard deviations used for weighting (cutoff, u)

269 and the anisotropy factor (a) that specifies the ellipticity of the kernel with positive values giving a more
270 horizontally-stretched shape. The two main parameters that control thresholding are the quantile (q) and
271 the offset factor (k). The interpolated surface estimate given by the ground follower has a resolution, R , and
272 provides increased resolution around rough surfaces by a factor of r . The increased resolution is triggered
273 by the roughness parameter, S , that specifies a standard deviation limit for the vertical distribution of
274 thresholded signal photons. Finally, the estimated depth of crevasses is controlled by the crevasse-quantile
275 parameter, Q . The specific parameter values we use in this analysis of Negribreen are given in Table 1.

276 **3.2. ICESat-2 ATLAS Data Processing with the DDA-ice**

277 We ran the DDA-ice on all ICESat-2 ATL03 data over Negribreen from January 2019 through 2020 using
278 the parameters from Table 1, which are close to the default parameters given in Herzfeld and others (2021),
279 but are optimized for the current analysis that spans multiple seasons and uses all the available beams.
280 The same parameter values were used for both the strong and the weak beams. We began by processing
281 all the strong beam data for a given cycle, which consists of three beams per pass with 9 passes (individual
282 RGTs) per cycle. After each run we manually filtered out all the cloudy data by looking at the DDA-ice
283 results so as to be sure that we retain only ice-surface signals.

284 For each beam pass we calculated the along-track “ice-signal fraction” as an indicator of the cloudiness of
285 each measurement pass over the Negribreen Glacier System (see Column 2 in Table S1 of the Supplementary
286 Material). The ice-surface fraction takes the length along-track for which a valid ice-surface height was
287 estimated and divides it by the total along-track survey length. The total along-track survey length (in
288 meters) for each beam pass over the Negribreen Glacier System is given in Column 3 of Table S1 of the
289 Supplementary Material.

symbol	meaning	value
s	standard deviation	3
u	cutoff	1
a	anisotropy	5
q	threshold quantile	0.75
k	threshold bias offset	0
l	slab thickness (m)	30
R	resolution of ground follower (m)	5
r	factor to reduce the R parameter	5
Q	crevasse depth quantile	0.5
S	standard deviation threshold of thresholded signal to trigger small step size in ground follower (m)	1.75

Table 1. DDA-ice parameters for Negribreen runs in this analysis. The same parameters were used for both the strong and weak beams. Ground-follower resolution when ice surface is rough: With $R = 5$ and $r = 5$, then the crevasse-follower resolution is 1 m.

290 Next, we processed all the weak-beam data for which the associated strong-beam pair yielded a non-
291 zero ice-signal fraction. Typically, the weak-beam data provided a non-zero ice-surface fraction when the
292 associated strong-beam data resulted in an ice-signal fraction greater than 0.9.

293 3.3. Surface Height Change Determination

294 We analyze ice-surface height change across each of the 54 ICESat-2 ground tracks across Negribreen in
295 2019 and 2020 in order to estimate mass transfer occurring during the surge evolution. At the resolution of
296 the DDA-ice interpolated ground estimate (1m or 5m), however, high-resolution morphology, especially
297 crevassing, complicates the bulk height change estimate. For example, fresh surge crevasses in upper
298 Negribreen (Fig. 3b), with depths up to 30 m, lead to an underestimation of the mean ice-surface height,
299 especially when ground follower resolution is refined over the crevasses. Height change analysis is further
300 complicated if the geophysical signal we are tracking corresponds to crevasse deepening or crevasses
301 advection. Compared to older and wider crevasses however, the cross-sectional area of the crevasse voids for
302 fresh crevasses is relatively small compared to the total width of the glacier. Therefore, for height-change
303 estimates in the case of young surge crevasses in upper Negribreen, we estimate surface height of the glacier
304 surface by using the 90th percentile height for every 30 m along-track bin.

305 Crevasses in lower Negribreen are more complex and have undergone several deformational processes at
306 this point in the surge. While originally they may have resembled the young crevasses in upper Negribreen,
307 large-scale dynamics near the front of the glacier have transformed these mature crevasses to appear
308 markedly different from those in Upper Negribreen as seen in Fig. 3c. Here, the cross-sectional area of
309 crevasse voids is significantly larger with respect to the total glacier width across-track. We therefore
310 calculate surface heights for height-change analysis in this region by taking the 50th percentile surface
311 height for every 30 m along-track bin. This gives the average surface height within the 30 m bin and
312 smooths out processes that change individual crevasse characteristics that may complicated surface height
313 change determination.

314 3.4. Roughness and Crevasse Characteristics

315 From ICESat-2/DDA-ice surface heights, vario functions are calculated to derive surface roughness values,
316 which are characteristic of the spatial structure of the ice surface (Herzfeld, 2008; Herzfeld and others, 2021).
317 Every 200 m along-track, we calculate discrete first-order vario function vectors, $\mathbf{v}^k = [v_1, \dots, v_j, \dots, v_N]$,
318 within 400 m windows centered at location x_k , which act on n pairs of height estimates, $z(x_i)$ and $z(x_i + h)$
319 separated by some lag distance h grouped in bins defined by the vector \mathbf{h} , whose bounds are indexed by j :

$$v_j^k = \frac{1}{2n} \sum_{i=1}^n (z(x_i) - z(x_i + h))^2 \quad (1)$$

where x_i is the along-track location of a height estimate (z) and h is the separation, or lag, distance between pairs of points with $h_{j-1} < h \leq h_j$, for $j = 1, \dots, N$, with $h_0 = 0$. We use $N = 10$ discrete lag distance bins of length 40 meters to characterize the surface at a given point x_k , implying $\mathbf{h} = [0, 40, 80, \dots, 400]$.

In cases where there are underlying regional trends in the data, such as a glacier's surface slope, it is more useful to use the residual vario function to quantify roughness (Herzfeld, 2008). Using the mean value m at a center point x_k , given by

$$m_j^k = \frac{1}{n} \sum_{i=1}^n (z(x_i) - z(x_i + h)) \quad (2)$$

the residual vario function V for a reference center point x_k is defined as

$$V_j^k = v_j^k - \frac{1}{2}m_j^k \quad (3)$$

where lag distance bins $h_{j-1} < h \leq h_j$, for $j = 1, \dots, N$ are used in both equations 2 and 3.

We derive an estimate of surface roughness, ζ_k , at point x_k by taking the maximum of \mathbf{V}^k :

$$\zeta(x_k) = \max(\mathbf{V}^k) \quad (4)$$

The parameter ζ is equivalent to the 1D *pond* parameter for a residual vario function (*respond*) introduced in Herzfeld (2008), though in the current analysis we refer to this quantity simply as roughness (of the glacier surface). This parameter is also derived using 2D (residual) vario functions applied to satellite imagery of Bering Glacier, Alaska, during surge in Trantow and Herzfeld (2018).

Additional crevasse and crevasse field characteristics, i.e. crevasse spacing and depth, are calculated from the DDA-ice height outputs for selected ICESat-2 tracks. Crevasse spacing and depth are determined using a simple deterministic algorithm (Herzfeld and others, 2013b, 2021, 2022) that identifies individual crevasses when the so called *jump_height* between crevasse top and crevasse bottom exceeds 2 meters.

3.5. Roughness Change Determination

We calculate mean rates of roughness change in 2019-2020 using the roughness measure, ζ , derived in Equation 4. While we are interested in the year-to-year dynamical component of roughness change, it is

340 important to consider its significant seasonal component. During the winter months of snow accumulation,
341 approximately October through April, crevasses of moderate and narrow widths can become covered, or
342 bridged, by snow. These snow-covered crevasses can persist throughout the summer in locations of low
343 deformation as seen in Fig. 3d. In this case, only the widest crevasses will be detected by the DDA-ice,
344 which finds the primary signal. The DDA-bifurcate-seaice algorithm (Herzfeld and others, 2023) is able to
345 detect secondary signals such as those beneath the water surface, but is not employed in this analysis as it
346 is not yet reliably adapted to land-ice applications. Because many crevasses are bridged by snow in winter,
347 analysis of roughness change is derived using data from summer months only when snow-bridges are the
348 least prevalent (roughly May through October). During peak melt season in July and August however,
349 crevasses exist that are filled with water at locations where the surge deformation has destroyed normal
350 englacial drainage paths that route water from the glacier surface to the base (see Fig. 3e) (Kamb and
351 others, 1985; Harrison and Post, 2003). Water-filled crevasses are present throughout the glacier system
352 but affect only a small number of the total crevasses (Herzfeld and others, 2022), and therefore should not
353 significantly affect the overall roughness estimates in this analysis.

354 4. RESULTS

355 4.1. Surface Height and Surface Height Change

356 4.1.1. Surface Heights and Data Coverage for each ICESat-2 Cycle

357 Along-track ice-surface height estimates yielded by the DDA-ice ground follower at 1-5 m resolution, as
358 determined by the algorithmic parameters in Table 1, are given for the four cycles in 2019 and the four
359 cycles in 2020 (Fig. 5). Heights in the Negribreen Glacier System range from ~ 0 m (sea-surface height)
360 at the terminus to over 800 m in the upper tributary glaciers. The most sparse coverage of the glacier
361 system occurs during the late-summer/autumn months (Fig. 5c,g), particularly in the lower part of the
362 glacier system, when low-level mixed-phase clouds have their highest occurrence (Shupe and others, 2011;
363 Gierens and others, 2020) (see photograph in Fig. 3a). During all but a couple cycles, Akademikarbreen
364 is more densely covered than Ordonnansbreen, likely due to the local orography, which strongly influences
365 the occurrence and characteristics of mixed-phase clouds (Gierens and others, 2020).

366 In general, clouds are the main factor controlling the ice-signal fraction for each beam pass and the survey
367 coverage for each ICESat-2 cycle. Optically thick clouds will fully attenuate ICESat-2 532 nm transmit
368 photons resulting in ice-signal fractions equal to zero, while optically thin clouds only partially attenuate the

369 transmit energy resulting in ice-signal fractions less than one (but possibly greater than 0). Therefore, the
 370 coverage maps shown in Fig. 5, along with quantified ice-signal fraction estimates given in the supplement,
 371 provide seasonal cloudiness information that are useful for airborne campaigns such as those conducted by
 372 Herzfeld and others (2022).

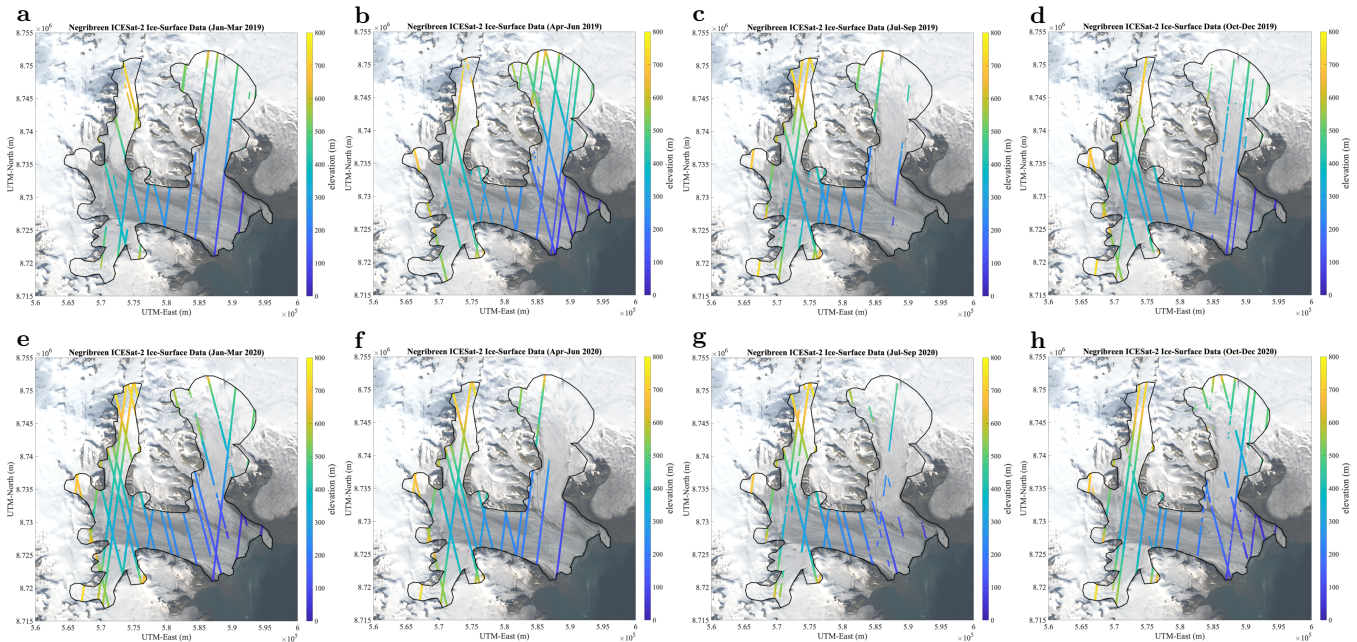


Fig. 5. Negribreen ice-surface height data from the DDA-ice for single ICESat-2 cycles (91 days). 2019 data (top row): (a) January-March 2019, (b) April-June 2019, (c) July-September 2019, (d) October-December 2019. 2020 data (bottom row): (e) January-March 2020, (f) April-June 2020, (g) July-September 2020, (h) October-December 2020.

373 4.1.2. Surface Height Rate of Change (2019-2020)

374 Fig. 6 gives the average surface height rate of change from 2019 to 2020 following the processes outlined
 375 in Section 3.3. While this calculation provides mean height changes in meters per year, it is important to
 376 note that the majority of the change occurs in the summer months, with very little height change between
 377 January and April. This is seen more clearly in the times series plots of Section 4.3.

378 Fig. 6 shows general thinning in the upper glacier above 5.85×10^5 m UTM-East and general thickening in
 379 the lower glacier below, implying a mass transfer from the upper glacier to the lower glacier. Surface heights
 380 grew between 2019 to 2020 in the front $\sim 1/3$ of the glacier at a rate reaching 30 ma^{-1} near Negribreen's
 381 terminus. A chaotic pattern of tightly spaced surface lowering and surface gains exceeding $\pm 30 \text{ ma}^{-1}$ near
 382 the center-front of the glacier reflects the generation and advection of massive and complex crevasses (see
 383 Fig. 3c).

384 Surface lowering occurs in the upper $\sim 2/3$ of Negribreen, while surface heights remain mostly constant
 385 on tributary glaciers such as Akademikarbreen and Rembebreen, which is seen clearly at the crossing of
 386 the medial moraines in Fig. 6. Aside from a slight lowering near its terminus, Ordonnansbreen also saw
 387 little changes in surface height from 2019 to 2020 despite the significant height changes that occurs just
 388 across the medial moraine on the surging Negribreen.

389 There is, however, a clear surface lowering of around 8 m a^{-1} on Transparentbreen, which connects
 390 Negribreen to the Filchnerfonna accumulation zone above the Negribreen Glacier System. Thus, the surge
 391 of Negribreen is affecting additional parts of the glacier system, expanding beyond the main glacier, across
 392 Transparentbreen and into the large catchment area above the glacier (Filchnerfonna). Transparentbreen
 393 appears to be the only tributary glacier in the Negribreen Glacier System experiencing significant height-
 394 change during the surge expansion from 2019 to 2020.

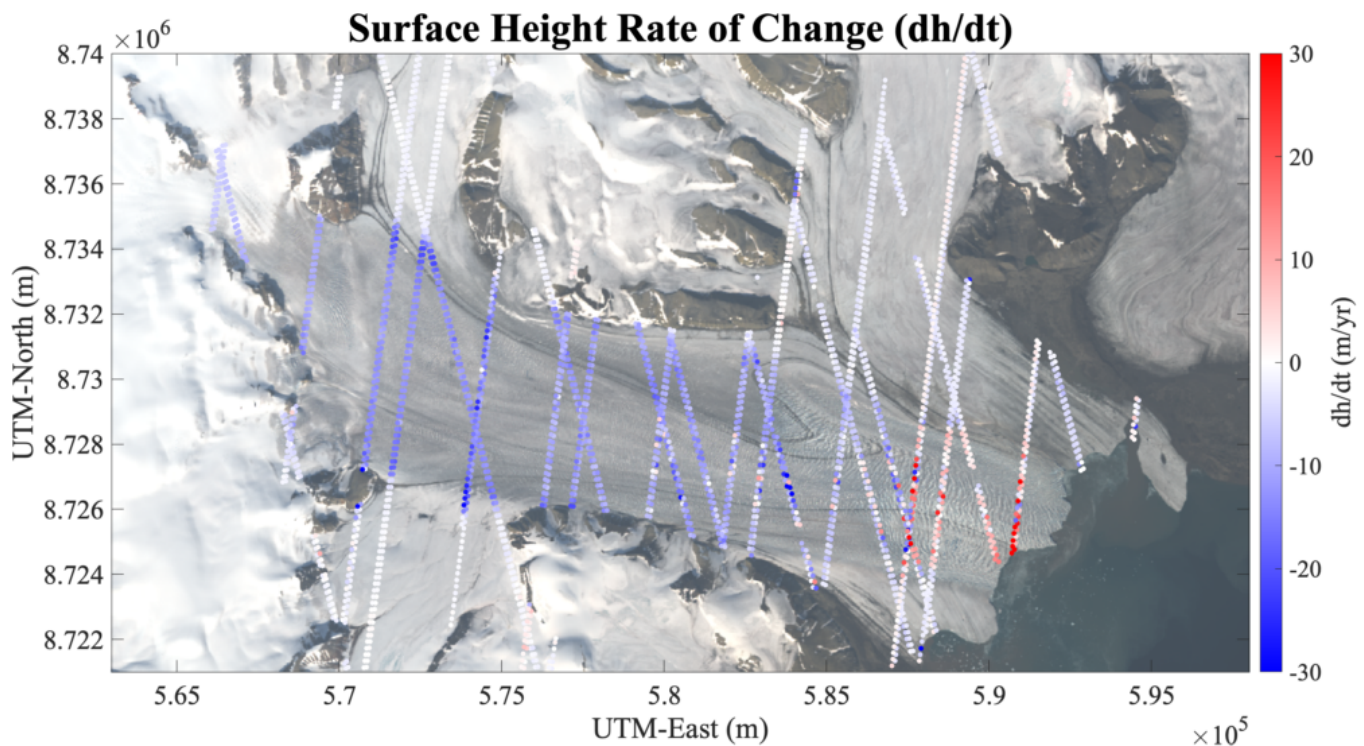


Fig. 6. Rates of change of glacier surface height during the 2019-2020 part of the recent Negribreen surge. Surface height change rate in meters per year.

395 4.2. Surface Roughness and Roughness Change

396 Crevassed regions are indicated by high surface roughness (Herzfeld, 2008; Herzfeld and others, 2014;
 397 Trantow and Herzfeld, 2018; Herzfeld and others, 2021, 2022). Negribreen's ice-surface roughness, given by
 398 ζ in Equation 4, for the four ICESat-2 cycles of 2019 and 2020 is shown in Fig. 7 and Fig. 8 respectively.

399 The medial moraines provide a clear boundary between the rough and surging Negribreen and the relatively
400 smooth surfaces of the non-surging tributary glaciers. In general, roughness is larger further downglacier as
401 the surging ice experiences more deformation events moving through the glacier system with the strongest
402 events experienced near the glacier front where surge velocities are largest (Fig. 4).

403 Changes in seasonal roughness characteristics, seen by comparing plots within Fig. 7 and Fig. 8, must be
404 interpreted with caution as seasonal effects, such as the loss of snow cover, are intertwined with dynamically-
405 induced roughness changes (see Section 3.5). With this in mind, we can use these maps to identify timing of
406 significant roughness changes. For example, we see persistent large roughness values along the Negribreen-
407 Rembebreen boundary beginning in the summer of 2019 ($\ln\zeta > 1$, Fig. 7c), indicating the timing of a
408 large surge-deformation event in the area. Similarly, we see a gradual increase in surface roughness at the
409 Negribreen-Akademikarbreen boundary with roughness estimates ($\ln\zeta$) growing from well below 0 in 2019
410 (Fig. 7), to eventually surpassing 1 by the summer of 2020 (Fig. 8c). The persistent roughness growth in
411 this area reflects the continued surge activity that occurs in upper Negribreen throughout 2019-2020.

412 Locations of surge activity are more clear in Fig. 9 which gives the mean rate of change of dynamically-
413 induced roughness over the 2019-2020 period of the Negribreen Glacier System surge following the approach
414 discussed in Section 3.5. Recall that Negribreen began accelerating in 2016 near the glacier front and surge-
415 induced changes have expanded upglacier as the surge phase matures (Haga and others, 2020; Herzfeld and
416 others, 2022). In Fig. 9 we see that for the most part, surface roughness has decreased in the lower glacier
417 reflecting reduced surge activity at that location. There are locations in the lower glacier however, that
418 have seen increased roughness indicating the continued occurrence of strong, but isolated, surge deformation
419 events.

420 In contrast, large portions of the upper glacier experienced increased roughness over the study time
421 interval (e.g., red regions in Fig. 9), which reflects the expansion of the surge upglacier in Negribreen. Large
422 increases in surface roughness also occurred on the ice falls between the Filchnerfonna and Negribreen, which
423 illustrates further expansion of surge effects beyond Negribreen and into the accumulation zone above the
424 glacier.

425 4.3. Time Series of ICESat-2 Surface Height Profiles

426 In this section, we analyze time series of selected ICESat-2 profiles that allow derivation of glaciological
427 changes associated with the surge of the Negribreen Glacier System in 2019-2020. We present a subset
428 ICESat-2 profiles, identified by their associated RGT and beam, based on the glaciological insight that

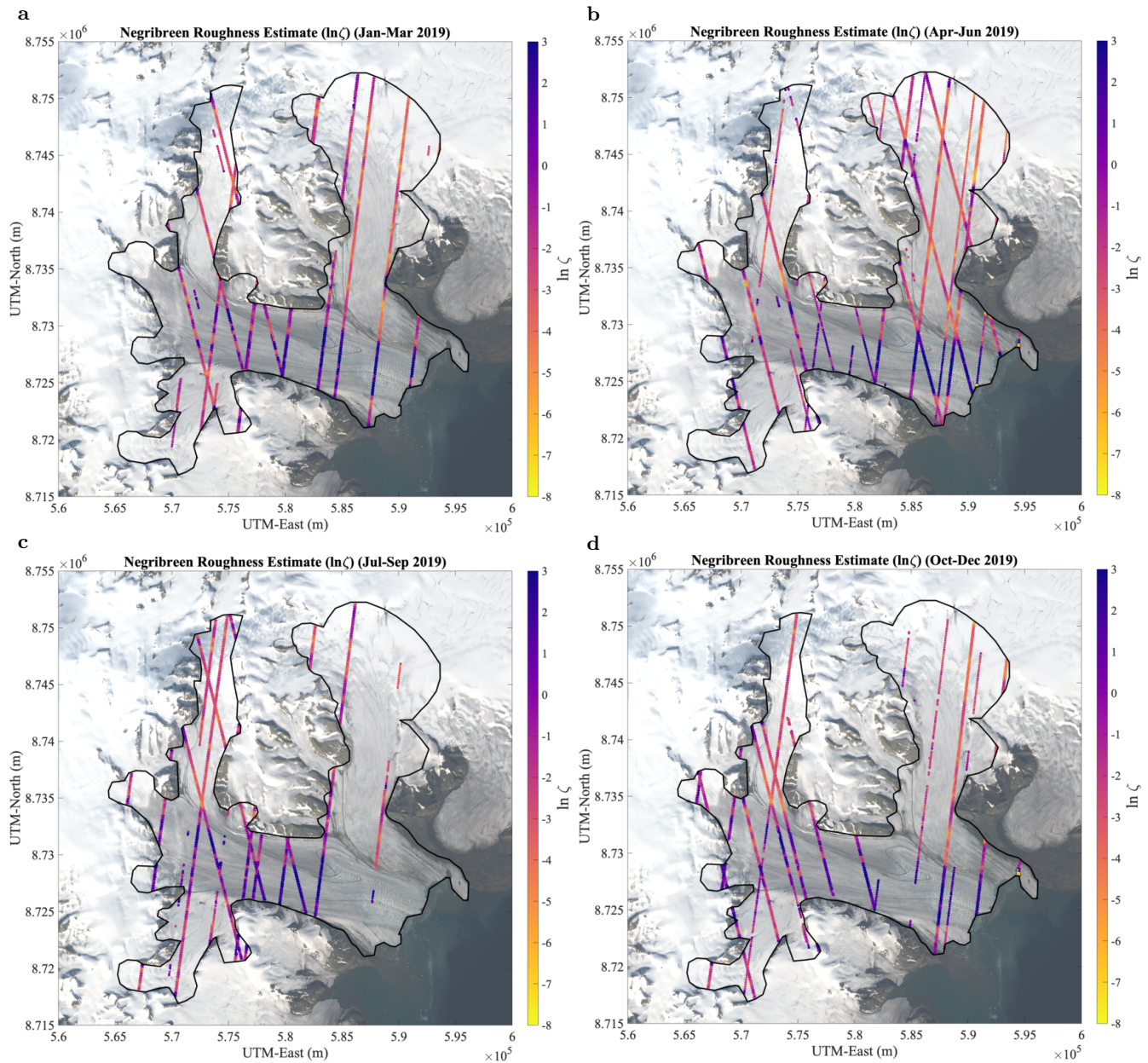


Fig. 7. 2019 Negribreen roughness data per cycle as given by the natural logarithm of the ζ parameter.

(a) January-March 2019, (b) April-June 2019, (c) July-September 2019, (d) October-December 2019.

429 their result provided. The full collection of ICESat-2 time series for each of the 54 ICESat-2 profiles can
 430 be found in the supplementary material (negri.change.suppl.pdf).

431 4.3.1. Detection of New Surge Crevasses and Changes in Existing Crevasse Fields

432 ICESat-2 data analyzed with the DDA-ice facilitate identification of crevasses (Herzfeld and others, 2017,
 433 2021, 2022). Here we utilize this crevasse detection capability to analyze and map the progression of the
 434 surge through the Negribreen Glacier System in 2019-2020.

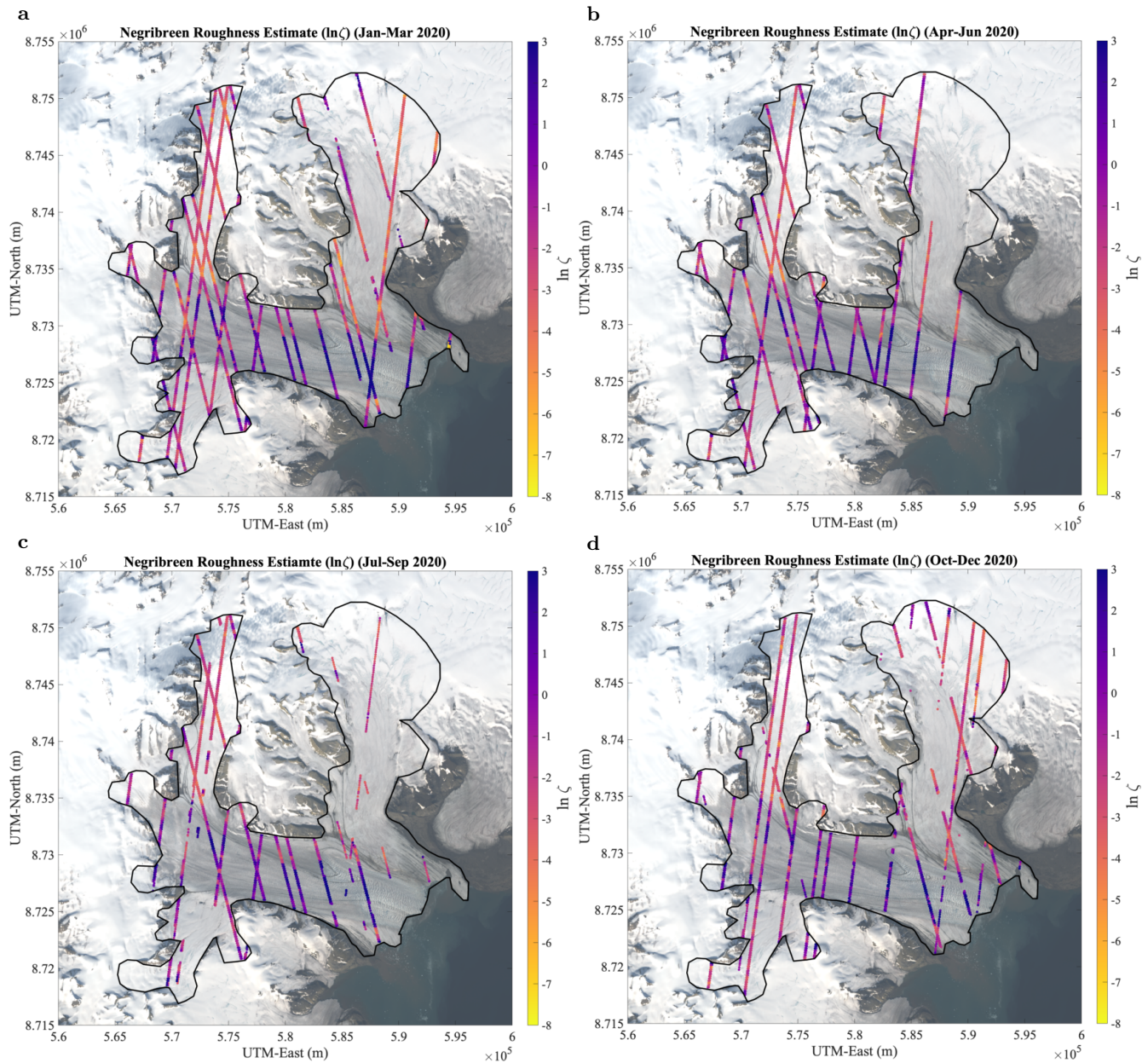


Fig. 8. 2020 Negribreen roughness data per cycle as given by the natural logarithm of the ζ parameter.

(a) January-March 2020, (b) April-June 2020, (c) July-September 2020, (d) October-December 2020.

435 All crevasse fields observed and analyzed here evolved morphologically through expansion or contraction,
 436 advection downglacier, formation of a snow-bridge and/or filling with water. An example of crevasse
 437 expansion is given by the occurrence of new crevasse fields formed in upper Negribreen along RGT 594 gt11
 438 as seen in Fig. 10a between 8.727 and 8.728×10^5 UTM-North where a smooth, uncrevassed ice-surface
 439 is reported in early 2019 (orange and yellow lines), and at the same location new crevasses have opened
 440 by November 2019 (green line). This particular finding indicates that additional crevasse fields formed in
 441 the southern part of upper Negribreen in late 2019, south of an existing larger crevasse field closer to the

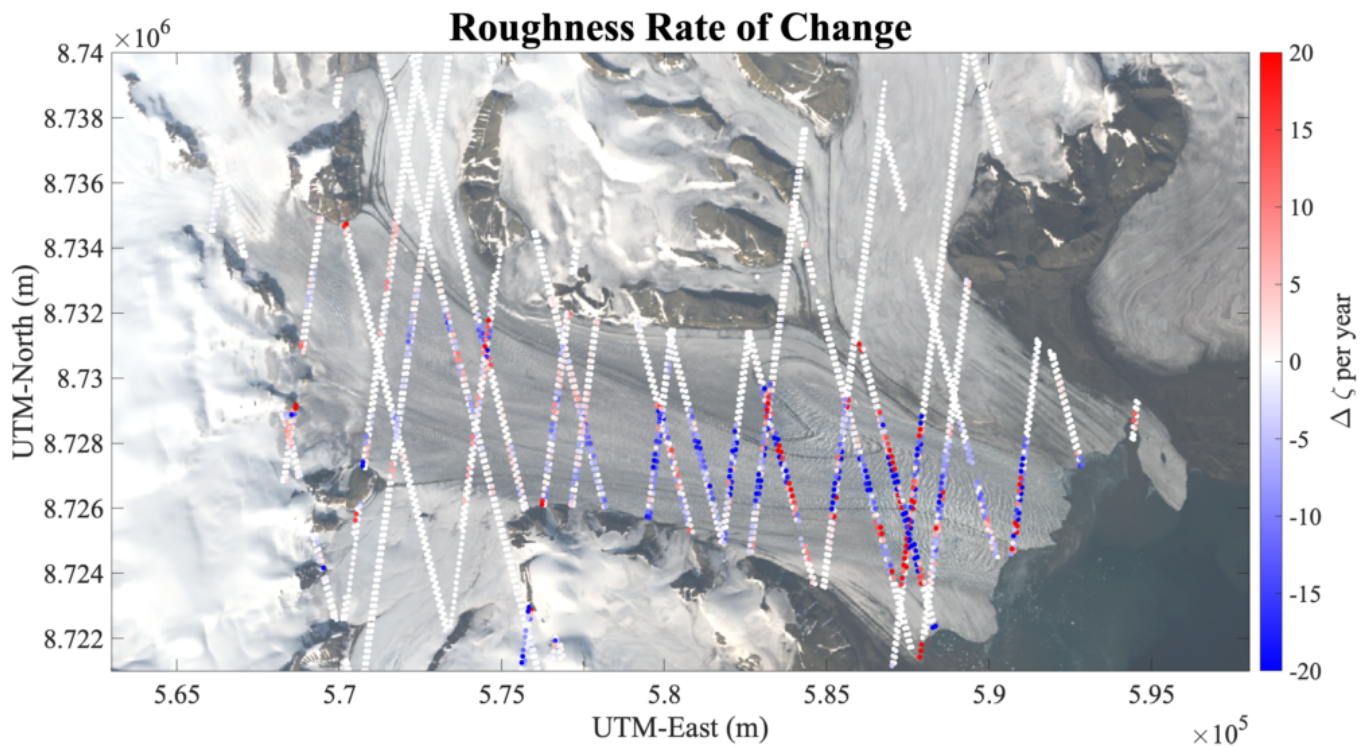


Fig. 9. Rates of change of roughness during the 2019-2020 part of the recent Negribreen surge. Roughness (ζ) change rate in $\Delta\zeta$ per year.

442 boundary with Akademikarbreen. Average crevasse spacing and maximal depth of crevasses along RGT
 443 594 gt1l near Akademikarbreen were estimated using airborne laser altimeter measurements during the
 444 field campaigns in 2018 and 2019, which matched estimates derived from ICESat-2 DDA-analyzed data
 445 (Herzfeld and others, 2021, 2022). Another example of the detection of crevasse expansion is found along
 446 RGT 594 gt2l in Fig. 10b near 8.726×10^5 m UTM-North where large crevasses formed along Negribreen's
 447 southern margin between February and April 2020.

448 Further evidence of the expansion in upper Negribreen is given by the time series of RGT 450 in Fig.
 449 11a-b. Large crevasses reaching 10 m depths near the southern margin (left-side of figure) formed in early
 450 2020 similar to those detected in the nearby RGT 594 data (Fig. 10). Note that beam-pair 1 of RGT 450
 451 is also surveyed and analyzed in Herzfeld and others (2022), which shows consistent detection of ~ 10 m
 452 deep crevasses in both the ICESat-2/DDA-ice and the airborne laser altimeter data in 2019. In addition,
 453 Fig. 11c, which shows RGT 152 gt3r, shows crevasse expansion across both the northern ($\sim 8.732 \times 10^5$
 454 UTM-North) and southern margin ($\sim 8.727 \times 10^5$ UTM-North) between early 2019 (orange line) and 2020
 455 (green, blue, brown lines). RGT 152 gt3r also presents an example of isolated crevassing and crevasse
 456 enlargement in the center of upper Negribreen near 8.729×10^5 m UTM-North.

457 The apparent disappearance of crevasses from 2019 to 2020, such as those in Fig. 10c near 8.729×10^5 m
458 UTM-North, may result from crevasse contraction, advection downglacier without upglacier replacement
459 of similar crevasses, snow-bridge formation or filling with water. Imagery may be used to determine the
460 exact process involved. The airborne photograph in Fig. 3a, taken near 8.729×10^5 m UTM-North, shows
461 that the crevasses under consideration, i.e. those found in and to the left of the medial moraine in the
462 image, have become bridged by snow.

463 Returning to RGT 594 gt11, we proceed to investigate changes in the width and depth of crevasses in
464 the large crevasse field seen in Fig. 10a between 8.730 and 8.732×10^5 UTM-North. Mean surface height
465 change (surface lowering) along this 2 km segment was -11.66 m between August 2019 and August 2020.
466 Mean crevasse spacing increased from 55.45 m to 57.6 m, mean depth decreased from 10.71 m to 9.82 m,
467 and maximum depth decreased from 16.01 m to 15.82 m. These changes in the crevasse characteristics are
468 typical of changes in crevasse fields that formed during earlier years of the surge in 2017 or 2018, as recorded
469 during our field campaigns. This result is consistent with the plot of Fig. 9 that reveals this region to be
470 the only one in upper Negribreen that saw a decrease in surface roughness from 2019 to 2020. Over time,
471 crevasses tend to widen a little, become shallower, and the crevasse edges are more rounded, as erosion
472 progresses (Herzfeld and others, 2013b).

473 In general, we find that the local maximum of crevasse depth increases from upglacier to downglacier
474 regions of Negribreen. From ~ 16 m depth along RGT 594 gt11 in upper Negribreen, maximal depths
475 increase to ~ 22 m near the mid-glacier along RGT gt3l (Fig. 10c) and exceed 30 m in the lower glacier
476 near the terminus.

477 *4.3.2. Surge Expansion Along and Across the Shear Margin*

478 The Negribreen-Akademikarbreen Medial Moraine (NAMM) is easily identified in airborne and satellite
479 imagery as the dark dividing line between the surging ice of Negribreen and the non-surging ice to the north.
480 From its formation point at the Negribreen-Akademikarbreen junction, the NAMM advects downglacier,
481 past the Lykkenhøgda hills at mid-glacier and along the Negribreen-Ordonnansbreen border in the lower
482 glacier, leaving an obvious stripe through Negribreen near its northern margin. The NAMM provides
483 an example of the folded moraine that can be used to identify a glacier as a surge glacier (Post, 1972;
484 Lefauconnier and Hagen, 1991). The fold results from a shift in the dynamic equilibrium between a surge
485 glacier (here, Negribreen) and a neighboring, non-surging glacier (Ordonnansbreen). The evolution of the
486 lower NAMM, along with its folds, are seen clearly in Fig. 2.

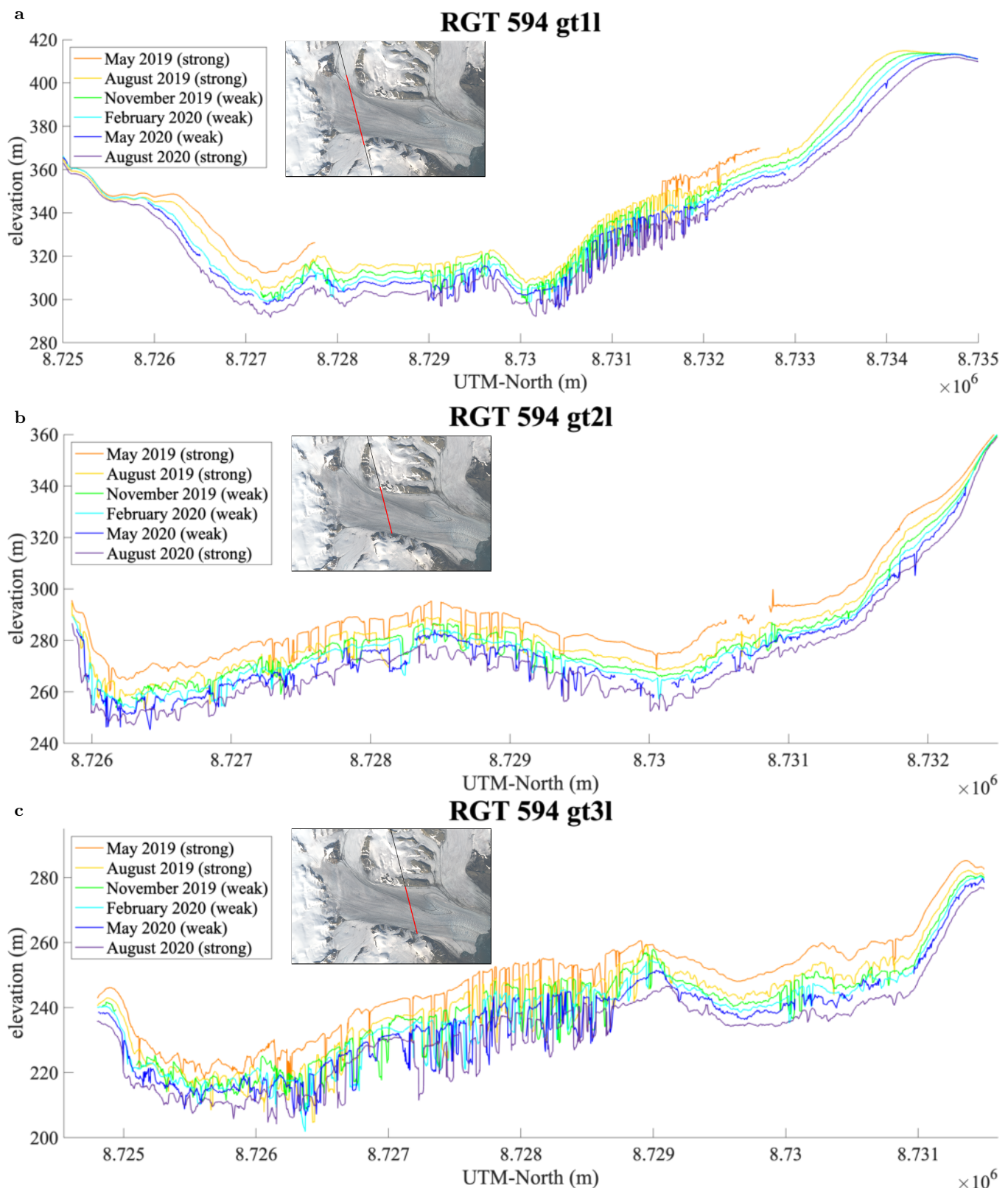


Fig. 10. DDA-ice results for RGT 594 over the Negribreen's major surge-affected area, 2019-2020. (a) RGT 594 gt1l, (b) RGT 594 gt2l, and (c) RGT 594 gt3l.

487 Throughout Negribreen's longitudinal extent, large shear stresses exist around the NAMM due to its
 488 boundary between the surging ice of Negribreen and the non-surging ice of the northern tributary glaciers.

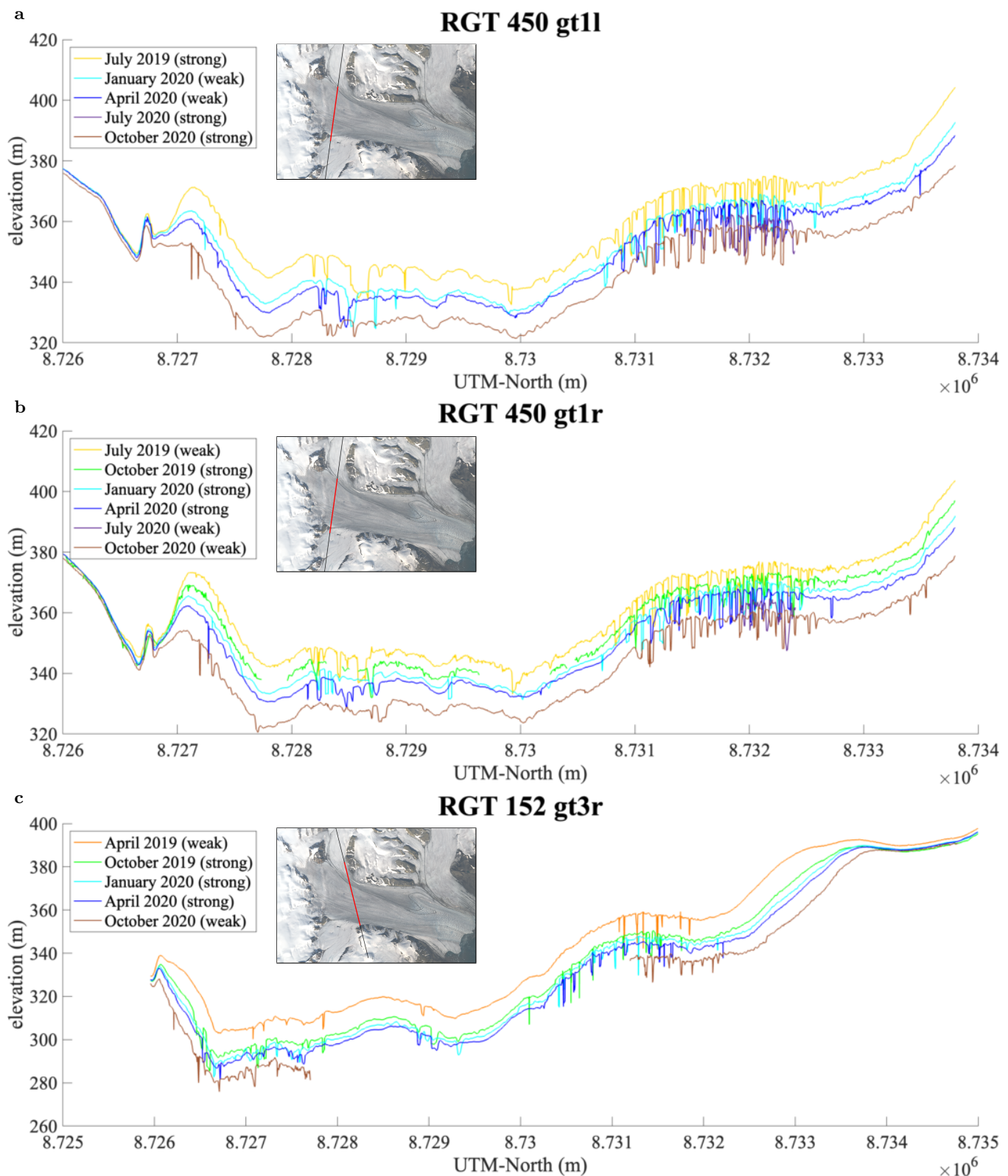


Fig. 11. Crevasse evolution in upper Negribreen as given by ICESat-2's RGT 450 and 152, 2019-2020. (a) RGT 450 gt1l, (b) RGT 450 gt1r and (c) RGT 152 gt3r.

489 In 2017 and 2018, Herzfeld and others (2022) documented the disintegration of the lower NAMM, i.e., the
490 Negribreen-Ordonnansbreen shear margin, along which the terminus retreated via processes of rifting and
491 calving at a pace faster than observed elsewhere in the glacier (visualized as a “retreating bay” at the
492 terminus). The formation of bays and melange areas occur at former areas of so-called chaotic crevasse
493 types (Herzfeld and others, 2013a), which are often found at locations with large shear stresses.

494 In the current analysis of surge progression, we detect the development of additional large crevasses in
495 northern Negribreen in the upper-mid glacier around the NAMM (i.e. upglacier of the largest “retreating
496 bay” observed in 2017) in 2020. Fig. 12 displays a transverse expansion of crevassing (outward toward the
497 NAMM), recorded in RGT 892 gt1l and gt1r. In August 2019 (yellow lines) deep crevasses (~ 10 m) are
498 measured across the majority of the glacier with a northern extent around 8.729×10^6 m UTM-North. By
499 August 2020 (purple lines), one year later, these large 10 m deep crevasses are seen to expand transversely
500 (northward) approximately 5 km to the extent of 8.7295×10^6 m UTM-North. These new crevasses appear
501 to be wider than the older ones to the south and are an indication of the intensification of the shear margin.

502 In August 2019, just before this noted crevasse expansion, large amounts of water were observed in the
503 crevasses near the northern NAMM as seen in Fig. 3f. The presence of clear blue meltwater in crevasses is
504 indicative of a local disruption in the englacial drainage system, which occurs in an actively surging region
505 (Kamb and others, 1985; Trantow and Herzfeld, 2024).

506 In Fig. 13, gt2l and gt2r of RGT 1334 show the same transverse (northern) expansion of crevassing across
507 the NAMM at the mid-glacier. The large 10 m deep crevasses expand toward the NAMM beginning at
508 8.7288×10^6 m UTM-North September 2019 (yellow lines), up to 8.7289×10^6 m UTM-North by June 2020
509 (blue lines) and to 8.729×10^6 m UTM-North by December 2020 (brown line, visible only in gt2l due to
510 partial cloud cover). Again, these changes are reflected in Fig. 9 where increased roughness is observed
511 from 2019 to 2020 at locations near the NAMM in upper Negribreen. Additional evidence of crevasse
512 expansion along and across the NAMM is given in Fig. 11c for RGT 152 gt3r which surveys Negribreen
513 just upglacier of RGT 1334 gt1l/r.

514 Our ICESat-2 results of fresh crevassing in mid and upper Negribreen around the NAMM indicate an
515 expansion of shear margin disintegration upglacier from a retreating bay at the terminus. Taken together,
516 the NAMM disintegration and the retreating bays at the terminus illustrate the evolution of a shear margin
517 with a very strong velocity gradient along a folded moraine (seen most starkly along the lower NAMM
518 in the velocity maps in Fig. 4). This result demonstrates how time series of ICESat-2 data, analyzed

519 with the DDA-ice, can be employed to derive quantitative information about complex surge processes,
 520 here, transverse deformation across a medial moraine forming a shear margin with increasingly large stress
 521 gradients as the surge evolves. To our knowledge, this is a new capability of satellite-based observation.

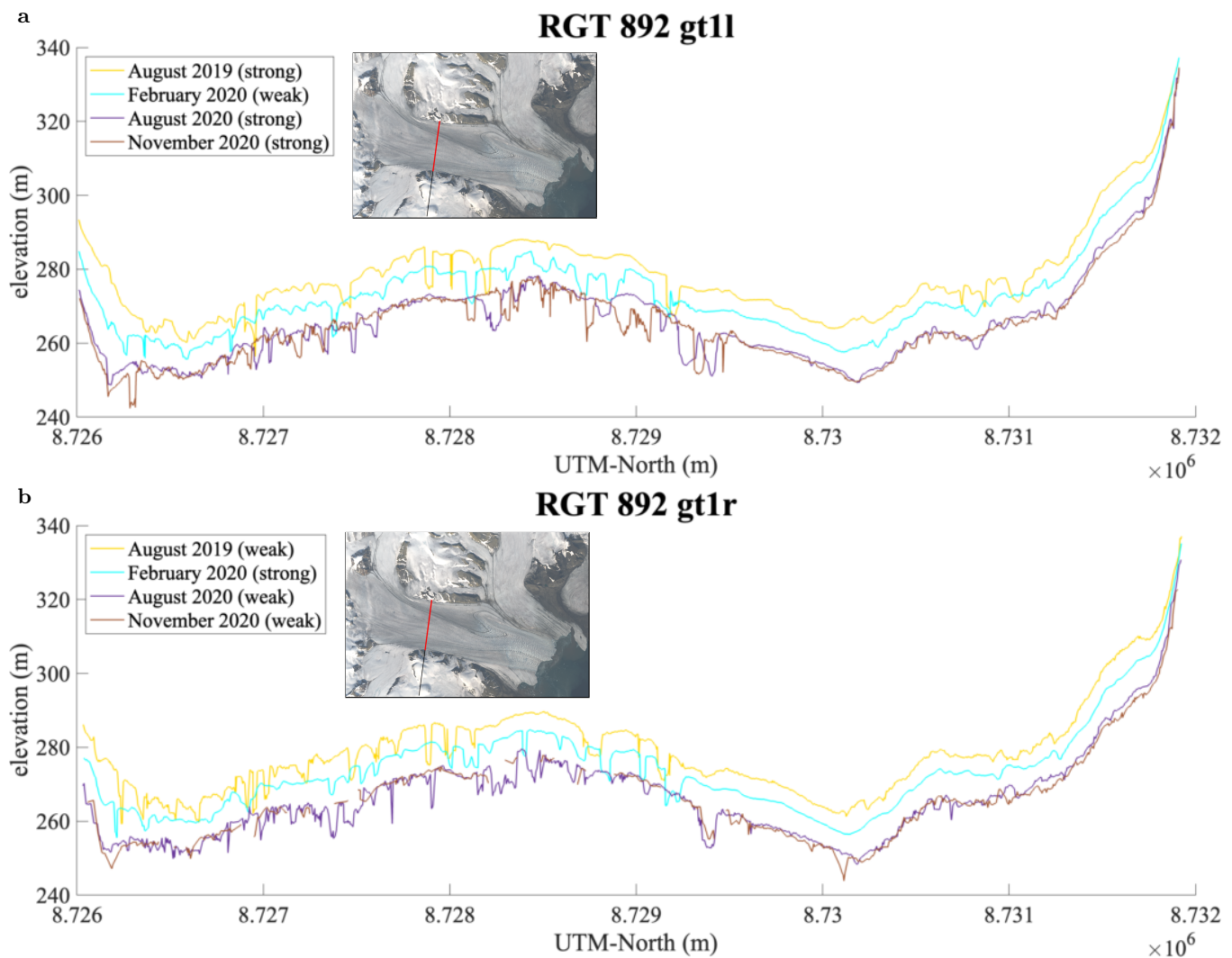


Fig. 12. DDA-ice results near the Negribreen-Akademikarbreen Medial Moraine (NAMM), 2019-2020. (a) RGT 892 gt1l, (b) RGT 892 gt1r.

522 4.3.3. Disintegration of the Ordonnansbreen Tooth

523 The Ordonnansbreen tooth, a small area of ice indicated by a black arrow in Fig. 2d, has been detaching
 524 from Ordonnansbreen's north terminus since the surge began in 2016. As noted earlier, Ordonnansbreen
 525 has been moving at quiescent speeds throughout our total observation time (2016-2021)), as seen in the
 526 velocity maps of Fig. 4.

527 The detaching tooth, along with the greater disintegration of the ice along the nearby medial moraine
 528 (lower NAMM), is visualized in the time series of Landsat-8 RGB imagery from 2018-2021 in Fig. 2. In

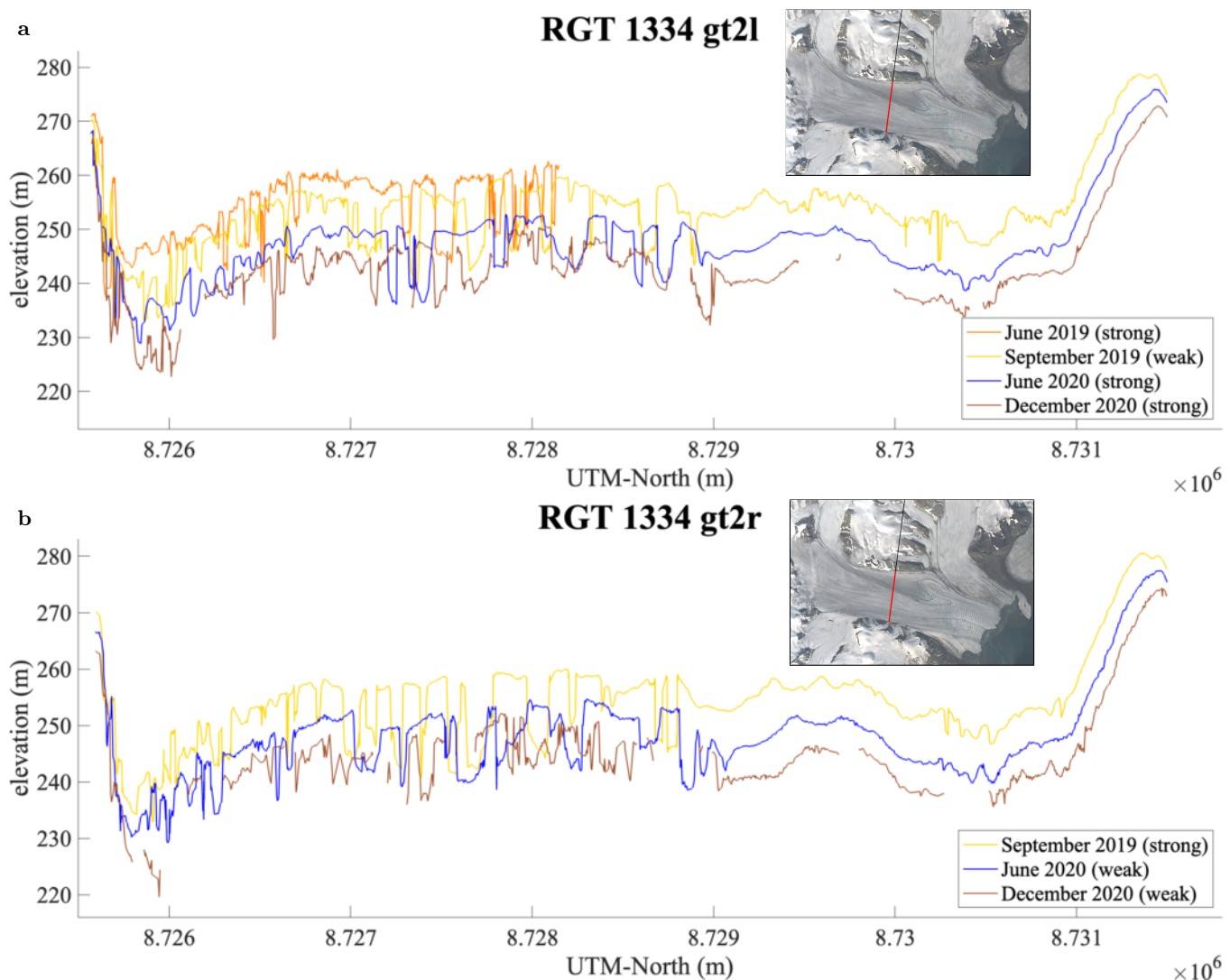


Fig. 13. DDA-ice results near the Negribreen-Akademikarbreen Medial Moraine (NAMM), 2019-2020. (a) RGT 1334 gt2l, and (b) RGT 1334 gt2r.

529 2018 (Fig. 2a) the tooth is attached to the northern part of the Ordonnansbreen terminus. The tooth's
 530 connection with the terminus shrinks by August 2019 (Fig. 2b) and becomes totally disconnected by July
 531 2020 (Fig. 2c). Ordonnansbreen's terminus rapidly retreats between July 2020 and August 2021 (Fig. 2d),
 532 greatly increasing the distance between the shore-fast tooth and the calving front. While the Landsat-8
 533 imagery helps visualize this process in two spatial dimensions, only with the ICESat-2 data do we get
 534 surface height and rifted-depth information to elucidate the third dimension of this rapidly changing
 535 glacial feature.

536 We see the separation of Ordonnansbreen's tooth in the time series of RGT 91 gt3l and gt3r (Fig. 14),
 537 which both cross the terminus of Ordonnansbreen. The orange line in Fig. 14, representing the ice-surface
 538 in April 2019, shows continuous ice extending from the shore line at 8.73×10^6 m UTM-North to the calving

539 front near 8.7274×10^6 m UTM-North. By January 2020, a ~ 10 m deep rift developed near 8.7299×10^6 m
540 UTM-North that penetrates all the way to the ocean surface, disconnecting the majority of the tooth from
541 the main glacier (see cyan-colored line in Fig. 14). The rift geometry at this location appears to have
542 remained relatively fixed between January 2020 (cyan) and July 2020 (purple, gt3l only) indicating little
543 surge activity during this time. By September 2020 (brown lines), the rift between Ordonnansbreen and the
544 tooth increased significantly from ~ 400 m to over 1.5 km in the direction of the RGT 91 survey line. The
545 September 2020 results in RGT 91 gt3r (Fig. 14b) in particular, indicate the presence of large icebergs and
546 an even greater separation distance nearing 5 km between the tooth and the main glacier. These results
547 indicate that the process of tooth detachment occurs most rapidly during peak glacier velocities in late
548 summer implying that the initial rift likely developed sometime around July or August 2019.

549 Looking at the entirety of the RGT 91 gt3l/r survey lines, we observe an ice-surface lowering of 4-
550 5 m across the Ordonnansbreen terminus during the 15 months between April 2019 and July 2020, i.e.,
551 approximately 20% of its total thickness, indicating rapid height and mass loss. This ice-surface continued
552 to lower by ~ 1 m across the entire width during the 3 months between July and September 2020. Therefore,
553 while the majority of Ordonnansbreen remains in a quiescent state, the Negribreen surge still has a
554 significant effect on the evolution of its neighboring tributary glacier through dramatic surface lowering,
555 rifting and calving at the terminus. The surge effects here, along with the major deformation along its
556 medial moraine with Negribreen (lower NAMM), leave the future state of Ordonnansbreen uncertain as
557 the Negribreen Glacier System surge continues to progress.

558 *4.3.4. Changes in the Ice Falls between the Filchnerfonna and Upper Negribreen*

559 The ice falls between Filchnerfonna and upper Negribreen have been areas of pervasive change during the
560 2019-2020 part of the surge in the Negribreen Glacier System, as observed during our 2019 field campaign
561 (Herzfeld and others, 2022). While ice falls are characterized by heavy crevassing due to steep topography,
562 the imprint of the surge manifests through fresh crevasse openings along with the widening and deepening of
563 existing crevasses. Fig. 15 and Fig. 16 show distinct signs of activity in the ice falls, indicative of expansion
564 of the surge-affected area beyond the Negribreen Glacier System. Increased crevassing is detected in the
565 southern ice falls (the largest of which is Filchnerfallet), particularly in 2020, but is not as prevalent along
566 Transparentbreen to the north (Fig. 15). There is less crevassing on Transparentbreen because it is less
567 steep than the other inflowing glaciers from Filchnerfonna, however, there is a pronounced surface lowering
568 across its entire width (Fig. 16). The rate of surface-height lowering here is increasing as seen by the spacing

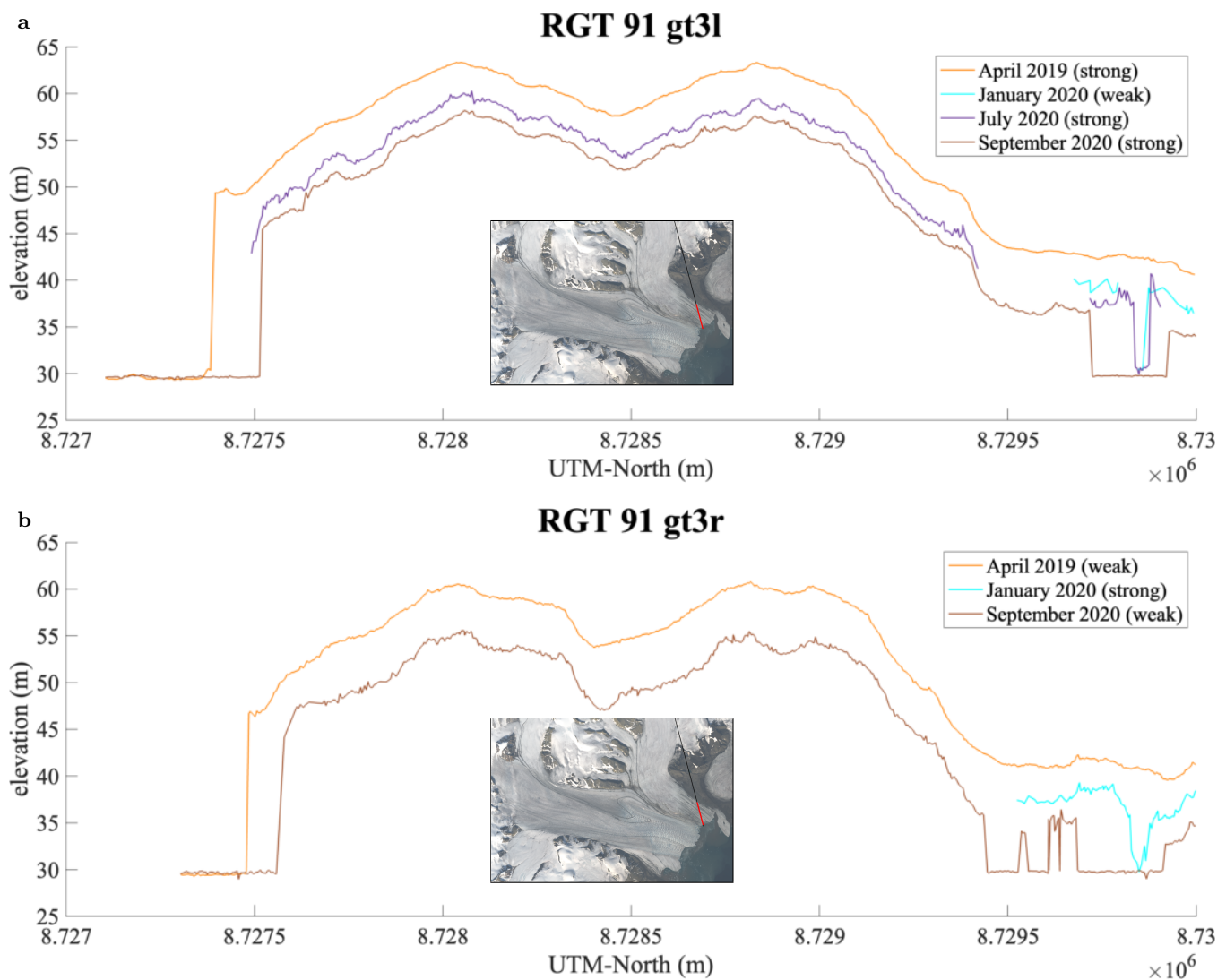


Fig. 14. DDA-ice results over Ordonnansbreen's terminus and the Ordonnansbreen tooth, 2019-2020. (a) RGT 91 gt3l shows the disintegration of Ordonnansbreen's terminus at its northern edge, i.e., at the tooth, above 8.729e6 UTM-North. (b) RGT 91 gt3r also displays the signal of a disintegrating northern terminus of Ordonnansbreen. Both time series also show significant surface lowering across the terminus width.

569 of the later 2020 lines (purple, brown) compared to the earlier 2019 lines (yellow, green), indicating building
 570 surge effects on Transparentbreen. In contrast, Filchnerfallet does not experience a clear signal of surface
 571 lowering until late 2020, which indicates delayed activation of ice flowing in from southern Filchnerfonna
 572 with respect to northern inflowing ice through Transparentbreen.

573 In the context of surge expansion beyond the Negribreen Glacier System, our results motivate the question
 574 of whether the surge in the Negribreen Glacier System may induce a disintegration of the surrounding
 575 glacial area, potentially destabilizing the Filchnerfonna. A less dramatic interpretation is that significant
 576 surface lowering in the Negribreen Glacier System leads to draw-down of ice flowing through the ice falls.

577 Either way, the surge in the Negribreen Glacier System is affecting adjacent ice areas at the border of its
 578 accumulation zone.

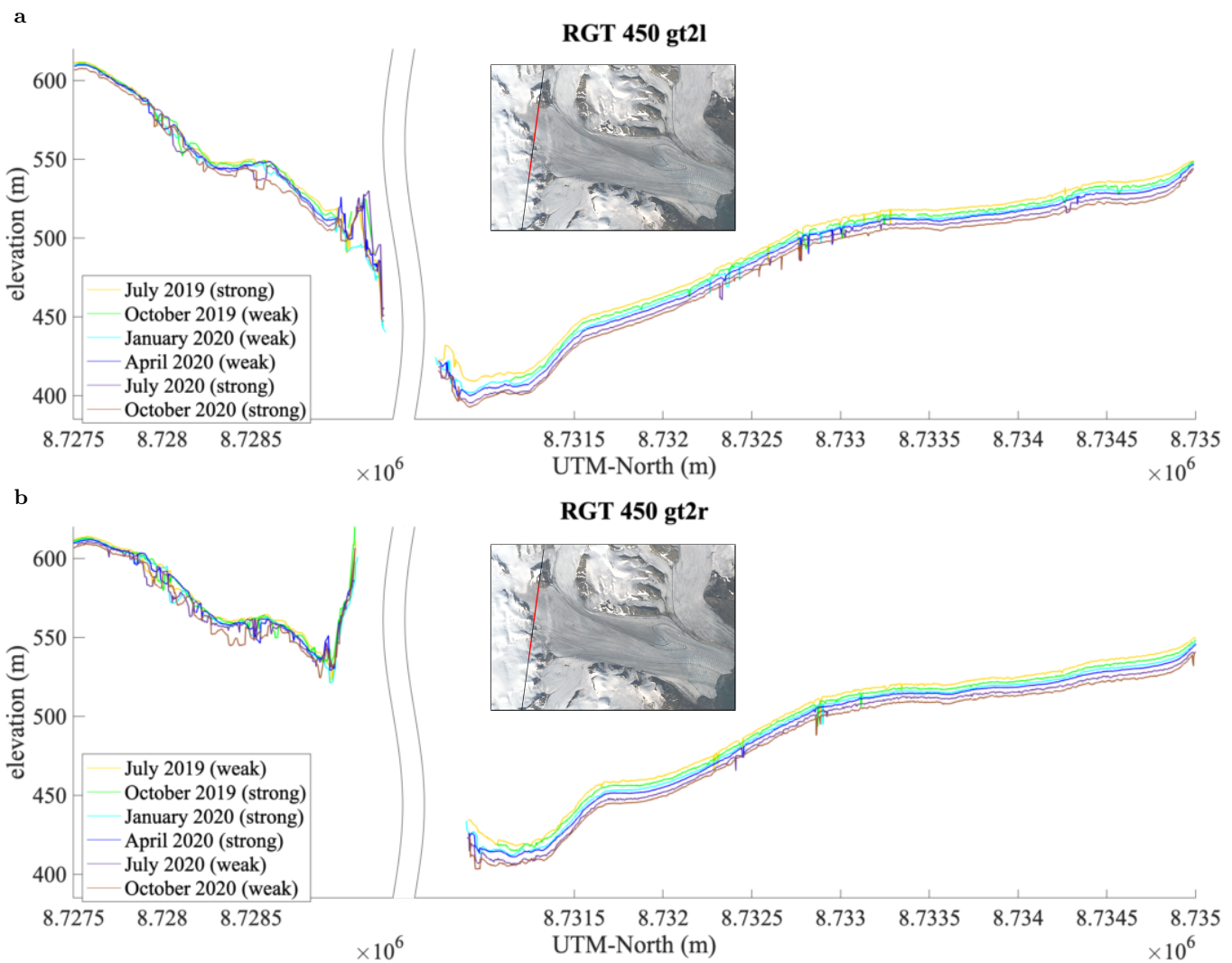


Fig. 15. DDA-ice results near the inflow from Filchnerfonna, 2019-2020. (a) RGT 450 gt2l surveying both the southern ice falls (Filchnerfallet) and Transparentbreen in the north and (b) RGT 450 gt2r surveying the ice falls (Filchnerfallet) and Transparentbreen.

579 4.3.5. Across-track Variability Between Strong and Weak Beam Pairs

580 To our knowledge, the DDA-ice is the only algorithm that can provide near-sensor resolution surface heights
 581 from both weak beam and strong beam data (Herzfeld and others, 2021), thereby facilitating investigation
 582 of the types of spatial changes that persist across the 90 m separation of the two beams in a pair. In
 583 the example of RGT 450 gt1l and gt1r (Fig. 11a and b), the older crevasse field between 8.7310×10^6 m
 584 UTM-North and 8.725×10^6 m UTM-North appears similar in both beams. However, the freshly opened
 585 crevasse field on the medial moraine in upper Negribreen that separates fast and slow flowing ice (8.728 -

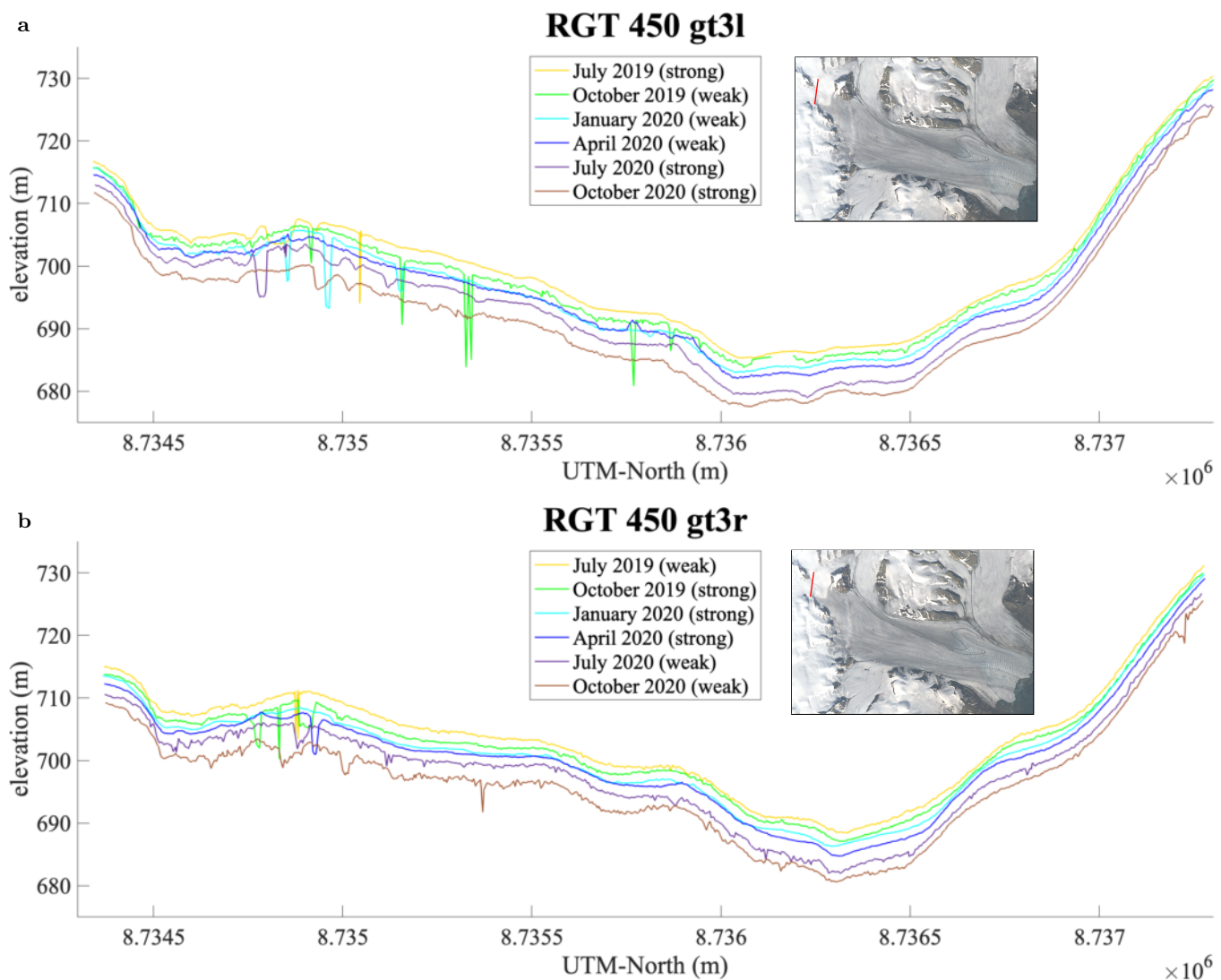


Fig. 16. DDA-ice results near the inflow from Filchnerfonna, 2019-2020. (a) RGT 450 gt3l surveying only Transparentbreen and (b) RGT 450 gt3r also surveying only Transparentbreen.

586 8.729×10^6 m UTM-North) is characteristically different in the two beams. RGT 450 gt1r, surveying 90 m
 587 further upglacier, captures a series of crevasses with similar depth whereas RGT 450 gt1l captures a
 588 particular large and wide crevasse (or rift) that lies in the moraine that separates two kinematic provinces.
 589 In particular, the acceleration and drawdown of ice flowing in through Transparentbreen to the north of
 590 the medial moraine lead to a discontinuity with the slower flowing ice from Filchnerfallet to the south (as
 591 seen in Fig. 15). The rift in the medial moraine, detected only in RGT 450 gt1l, is moving southward as
 592 the surge progresses, which indicates when the regime of fast flowing ice extends across a larger part of the
 593 glacier.

594 Fig. 12 gives a second example of the across-track variability between beam pairs. The crevasse field
 595 around 8.729×10^6 m UTM-North is characteristically different in August 2020 (purple line) and November

596 2020 (brown line) between the two beams, with the strong beam (gt1l) detecting more and larger crevasses
597 than the weak beam (gt1r) that lies 90 m upglacier. This result points to the large spatial variability in
598 crevasse characteristics along the NAMM which divides fast and slow moving ice.

599 In summary, analysis of across-track variability between ICESat-2 beam pairs provides spatial information
600 at the 90 m length scale, which is on the order of individual crevasse fields (Herzfeld and others, 2021).
601 Therefore, this information can be complementary to image classification of crevasse provinces using
602 machine learning approaches, e.g., Herzfeld and others (2024). In addition, this type of analysis can also
603 inform design of beam geometries for future high resolution lidar missions.

604 *4.3.6. General Mass Transfer Observations*

605 The surface height changes of 2019-2020 given by Fig. 6 reflect significant mass transfer from the reservoir
606 area in upper and mid Negribreen downglacier to the receiving area in the lower glacier within 5 km of
607 the terminus. The ice-mass transferred to the receiving area is eventually transported to the Arctic Ocean
608 via heavy calving during the surge. These mass transfer observations are further detailed in the analysis of
609 surface height time series of the preceding sections.

610 In total, the ICESat-2 results give a clear indication that the mass transfer is surge-induced rather than
611 climatically induced. As seen most clearly in Fig. 10a and Fig. 11b, surface height profiles overlie each
612 other at the beginning and end of each track (i.e., on the non-surging tributary glaciers on the sides of
613 Negribreen) but significant height change is apparent along the interior of the profile. If surface lowering
614 were climatically caused (mass loss through melting), then similar height changes between 2019 and 2020
615 would be observed across the entire profile.

616 **5. CONCLUSIONS**

617 In this paper, we have derived information on geophysical processes that occurred during the surge of
618 Negribreen Glacier System based on analysis of 2 years of ICESat-2 ATLAS data from 2019 and 2020,
619 processed with the DDA-ice. ICESat-2 data, analyzed with the DDA-ice, provide a unique and novel
620 capability to obtain geophysical information on high resolution height changes during a glacier surge
621 from spaceborne altimeter observations. The Negribreen Glacier System provides an ideal study region,
622 as the main acceleration phase of the surge overlaps with the observation phase of the ICESat-2 mission.
623 Negribreen's surge started in 2016, with peak acceleration in 2017, while ICESat-2 was launched on 15
624 September 2018. Here we have analyzed all ICESat-2 data collected between January 2019 and December

625 2020 over Negribreen to demonstrate our approach. The analysis is supplemented by velocity maps from
626 Sentinel-1 SAR imagery and airborne data from our August 2019 campaign to Negribreen.

627 Geophysical information on the evolution of the surge is derived from the ICESat-2/DDA-ice high
628 resolution data, including: crevassing, height changes, mass transfer toward the terminus and roughness
629 changes indicative of evolving crevasse fields. Height-change rates in 2019-2020 range from -30 ma^{-1} in
630 the reservoir areas of upper Negribreen, to $+30 \text{ ma}^{-1}$ in the receiving area in the lower glacier near the
631 terminus. Roughness change maps indicate an expansion of the surge in upper Negribreen, particularly
632 near the shear margins, while surge activity in the lower glacier lessened from 2019 to 2020.

633 Time series analysis of ICESat-2 profiles, analyzed with the DDA-ice, indicates formation of new crevasse
634 fields and expansion of existing crevasse fields, as the surge progresses and affects larger areas of the
635 Negribreen Glacier System. The increased surge activity from 2019 to 2020 in the upper glacier is especially
636 seen on the inflowing glaciers from the Filchnerfonna accumulation zone, and along the Negribreen-
637 Akademikarbreen Medial Moraine, which divides the surging ice of Negribreen and the non-surging ice
638 of the northern tributary glaciers. This later observation, together with the outward crevasse expansion
639 observed along the southern moraine that separates fast and slow ice, implies an increased zone of actively
640 surging ice across the glacier width as the surge progresses into its mature state.

641 The fresh surge crevassing along and across the NAMM in the mid and upper glacier in 2019-2020
642 indicates disintegration along the shear margin and reflects a continuation of the deformational process
643 that resulted in a “retreating bay,” an area of open water filled with melange that formed as a result of
644 a strong force gradient along the shear margin between the surging ice of Negribreen and non-surging ice
645 of neighboring Ordonnansbreen, near the terminus in 2017. Occurrence of water in crevasses that reaches
646 almost to the ice surface height was observed near the upper NAMM in August 2019, just before the new
647 crevasses were formed. Furthermore, our analysis of surge progression in 2019-2020 provided detailed height
648 information on the separation process of a segment of lower Ordonnansbreen (“Ordonnansbreen tooth”)
649 from the main glacier along a rift that had formed during the surge.

650 Large-scale mass transfer, extensive roughness changes, and the striking disintegration along the NAMM,
651 and of Ordonnansbreen’s tooth and the lower glacier as a whole, clearly illustrate the rapid surface change
652 and mass loss a glacier can experience during a surge. These results demonstrate the novel capability of
653 ICESat-2, analyzed with the DDA-ice, to provide high-resolution height data capable of documenting these
654 complex surge processes from space.

655 SUPPLEMENTAL MATERIAL

656 The supplementary material for this article can be found at github.com/trantow/negri.change.supplement.

657 DATA AVAILABILITY

658 (1) ICESat-2 data products, e.g. ATL03, are freely available through NASA at <https://earthdata.nasa.gov/>
659 (release 4 used in this paper) and is provided by the National Snow and Ice Data Center (NSIDC).
660 (2) Data collected as part of the Negribreen Airborne Geophysical Campaigns, collected by the
661 authors and their extended team, are available through the NSF Arctic Data Center and can be
662 accessed at <https://arcticdata.io/data/10.18739/A2QF8JK7T> (Herzfeld and Trantow, 2021). (3) Sentinel-
663 1 SAR data are freely available through the European Space Agency's Copernicus Open Access Hub
664 (<https://scihub.copernicus.eu/>). (4) Landsat-8 data are freely available through the U.S. Geological Survey,
665 e.g., through the USGS Global Visualization Viewer (GloVis) (<https://glovis.usgs.gov/>).

666 ACKNOWLEDGEMENTS

667 Thanks are due to our pilot and technician, Harald Sandal and Gustav Svanstrom, Airlift, Norway, of
668 the 2019 Negribreen campaign, to Matt Lawson, Geomathematics Group, University of Colorado Boulder,
669 for help with data collection in 2019, to our dearly missed colleague Chris Borstad, University Center in
670 Svalbard (UNIS), then University of Montana, to Jack Kohler, Geir Ove Aspnes, Jørn Dybdahl, Norwegian
671 Polar Institute, to Thomas Nylen and UNAVCO Boulder for GPS support, to Inger Jennings (SIOS)
672 and Kristin Woxholth, Longyearbyen, for help with logistical support, to the ICESat-2 Project, especially
673 Thomas Neumann, Kaitlin Harbeck, David Hancock and Anthony Martino for collaboration and support
674 regarding ICESat-2, to Huilin Han and Rachel Middleton, Geomathematics Group, University of Colorado
675 Boulder, for derivation of some of the velocity maps from Sentinel-1 SAR data and to the European Space
676 Agency for providing the SNAP tool for velocity-map calculation.

677 Research and data collection were supported by the U.S. National Aeronautics and Space Administration
678 (NASA) Earth Sciences Division under awards 80NSSC20K0975, 80NSSC18K1439 and NNX17AG75G and
679 by the U.S. National Science Foundation (NSF) under awards OPP-1745705 and OPP-1942356 (Office of
680 Polar Programs) and OAC-1835256 (Office of Advanced Cyberinfrastructure); Principal Investigator for
681 all awards is Ute Herzfeld. The helicopter was provided by the Norwegian Polar Institute and operated
682 by Airlift. Collection of airborne data was conducted with permission of the National Security Authority

683 of Norway, the Civil Aviation Authority of Norway and the Governor of Svalbard, registered as Research
684 in Svalbard Project RIS-10827 “NEGRIBREEN SURGE”. The data collection was also partly supported
685 through a 2018 Access Pilot Project (2017_0010) of the Svalbard Integrated Observing System (SIOS). All
686 this support is gratefully acknowledged.

687 REFERENCES

- 688 Banerjee D, Garg V and Thakur PK (2022) Geospatial investigation on transitional (quiescence to surge initiation)
689 phase dynamics of Monacobreen tidewater glacier, Svalbard. *Advances in Space Research*, **69**(4), 1813–1839
- 690 Benn D, Fowler AC, Hewitt I and Sevestre H (2019) A general theory of glacier surges. *Journal of Glaciology*, **65**(253),
691 701–716
- 692 Bhambri R, Hewitt K, Kawishwar P and Pratap B (2017) Surge-type and surge-modified glaciers in the Karakoram.
693 *Scientific Reports*, **7**(1), 15391
- 694 Björnsson H, Pálson F, Siggurdsson O and Flowers G (2003) Surges of glaciers in Iceland. *Annals of Glaciology*, **36**,
695 82–90
- 696 Chen D and 14 others (2021) *Climate Change 2021: The Physical Science Basis. Contribution of Working Group I to*
697 *the Sixth Assessment Report of the Intergovernmental Panel on Climate Change*, 147–286. Cambridge University
698 Press, Cambridge, United Kingdom and New York, NY, USA
- 699 Clarke G (1987) Fast glacier flow: Ice streams, surging, and tidewater glaciers. *Journal of Geophysical Research*, **92**,
700 8835–8842
- 701 Dolgushin L and Osipova G (1975) Glacier surges and the problem of their forecast. *Symposium on Snow and Ice in*
702 *Mountain Regions, IAHS Publication*, **104**, 292–304
- 703 Dowdeswell J, Drewry D, Liestøl O and Orheim O (1984) Radio echo-sounding of Spitsbergen glaciers: problems in
704 the interpretation of layer and bottom returns. *Journal of Glaciology*, **30**(104), 16–21
- 705 Dunse T, Schellenberger T, Hagen J, Kääb A, Schuler TV and Reijmer C (2015) Glacier-surge mechanisms promoted
706 by a hydro-thermodynamic feedback to summer melt. *The Cryosphere*, **9**(1), 197–215
- 707 Flowers GE, Roux N, Pimentel S and Schoof CG (2011) Present dynamics and future prognosis of a slowly surging
708 glacier. *The Cryosphere*, **5**, 299–313
- 709 Geudtner D, Torres R, Snoeij P, Davidson M and Rommen B (2014) Sentinel-1 system capabilities and applications.
710 In *Geoscience and Remote Sensing Symposium (IGARSS), 2014 IEEE International*, 1457–1460, IEEE
- 711 Gierens R, Kneifel S, Shupe MD, Ebell K, Maturilli M and Löhnert U (2020) Low-level mixed-phase clouds in a
712 complex Arctic environment. *Atmospheric Chemistry and Physics*, **20**(6), 3459–3481

- 713 Goerlich F, Bolch T and Paul F (2020) More dynamic than expected: an updated survey of surging glaciers in the
714 Pamir. *Earth System Science Data*, **12**(4), 3161–3176
- 715 Guan W and 7 others (2022) Updated surge-type glacier inventory in the West Kunlun Mountains, Tibetan Plateau,
716 and implications for glacier change. *Journal of Geophysical Research: Earth Surface*, **127**(1), e2021JF006369
- 717 Guillet G and 6 others (2022) A regionally resolved inventory of High Mountain Asia surge-type glaciers, derived
718 from a multi-factor remote sensing approach. *The Cryosphere*, **16**(2), 603–623
- 719 Haga ON, McNabb R, Nuth C, Altena B, Schellenberger T and Kääh A (2020) From high friction zone to frontal
720 collapse: dynamics of an ongoing tidewater glacier surge, Negribreen, Svalbard. *Journal of Glaciology*, **66**(259),
721 742–754
- 722 Harrison W and Post A (2003) How much do we really know about glacier surging? *Annals of Glaciology*, **36**(1), 1–6
- 723 Herzfeld U, McDonald B and Weltman A (2013a) Bering Glacier and Bagley Ice Valley surge 2011: Crevasse
724 classification as an approach to map deformation stages and surge progression. *Annals of Glaciology*, **54**(63),
725 279–286
- 726 Herzfeld U, Trantow T, Lawson M, Hans J and Medley G (2021) Surface heights and crevasse types of surging
727 and fast-moving glaciers from ICESat-2 laser altimeter data — Application of the density-dimension algorithm
728 (DDA-ice) and validation using airborne altimeter and Planet SkySat data. *Science of Remote Sensing*, **3**, 1–20
- 729 Herzfeld U, Trantow T, Buckley E, Farrell S and Lawson M (2023) Automated detection and depth measurement of
730 melt ponds on sea ice from ICESat-2 ATLAS data — the DDA-bifurcate-seaice. *IEEE Transactions of Geoscience
731 and Remote Sensing*, 1–16
- 732 Herzfeld UC (2008) Master of the obscure — Automated geostatistical classification in presence of complex
733 geophysical processes. *Mathematical Geosciences*, **40**(5), 587–618
- 734 Herzfeld UC and Mayer H (1997) Surge of Bering Glacier and Bagley Ice Field, Alaska: an update to August 1995
735 and an interpretation of brittle-deformation patterns. *Journal of Glaciology*, **43**(145), 427–434
- 736 Herzfeld UC and Trantow T (2021) Airborne Laser Altimeter, Global Positioning System (GPS), Inertial
737 Measurement Unit (IMU) and Imagery Campaign of the Surging Negribreen Glacier, Svalbard, in July 2017
738 and July 2018. <https://arcticdata.io/catalog/view/doi:10.18739/A23J39249>
- 739 Herzfeld UC, McDonald B, Stachura M, Hale RG, Chen P and Trantow T (2013b) Bering Glacier surge 2011: Analysis
740 of laser altimeter data. *Annals of Glaciology*, **54**(63), 158–170
- 741 Herzfeld UC and 9 others (2014) Elevation changes and dynamic provinces of Jakobshavn Isbræ, Greenland, derived
742 using generalized spatial surface roughness from ICESat GLAS and ATM data. *Journal of Glaciology*, **60**(223),
743 834–848

- 744 Herzfeld UC, Trantow TM, Harding D and Dabney PW (2017) Surface-height determination of crevassed glaciers –
745 Mathematical principles of an autoadaptive density-dimension algorithm and validation using ICESat-2 simulator
746 (SIMPL) data. *IEEE Transactions on Geoscience and Remote Sensing*, **55**(4), 1874–1896
- 747 Herzfeld UC, Lawson M, Trantow T and Nylen T (2022) Airborne Validation of ICESat-2 ATLAS Data over Crevassed
748 Surfaces and Other Complex Glacial Environments: Results from Experiments of Laser Altimeter and Kinematic
749 GPS Data Collection from a Helicopter over a Surging Arctic Glacier (Negribreen, Svalbard). *Remote Sensing*,
750 **14**(5), 1185
- 751 Herzfeld UC, Hessburg LJ, Trantow TM and Hayes AN (2024) Combining “Deep Learning” and Physically
752 Constrained Neural Networks to Derive Complex Glaciological Change Processes from Modern High-Resolution
753 Satellite Imagery: Application of the GEOCLASS-image System to Create VarioCNN for Glacier Surges. *Remote*
754 *Sensing*, **16**(11), 1854
- 755 Jiskoot H (2011) Glacier surging. In PS Vijay P Singh and UK Haritashya (eds.), *Encyclopedia of Snow, Ice and*
756 *Glaciers*, 415–428, Springer Science & Business Media
- 757 Jiskoot H, Murray T and Luckman A (2003) Surge potential and drainage-basin characteristics in East Greenland.
758 *Annals of Glaciology*, **36**, 142–148
- 759 Kääb A, Bazilova V, Leclercq PW, Mannerfelt ES and Strozzi T (2023) Global clustering of recent glacier surges
760 from radar backscatter data, 2017–2022. *Journal of Glaciology*, 1–9
- 761 Kamb WB and 7 others (1985) Glacier surge mechanism: 1982–1983 surge of Variegated Glacier, Alaska. *Science*,
762 **227**(4686), 469–479
- 763 Kamb WB (1987) Glacier Surge Mechanism Based on Linked Cavity Configuration of the Basal Water Conduit
764 System. *Journal of Geophysical Research*, **92**(B9), 9083–9100
- 765 Kochtitzky W and 9 others (2020) Climate and surging of Donjek glacier, Yukon, Canada. *Arctic, Antarctic, and*
766 *Alpine Research*, **52**(1), 264–280
- 767 Lefauconnier B and Hagen JO (1991) Surging and calving glaciers in eastern Svalbard. *Meddelelser, Norsk*
768 *Polarinstitutt*, **116**, 1–133
- 769 Liu J, Enderlin EM, Bartholomaus TC, Terleth Y, Mikesell TD and Beaud F (2024) Propagating speedups during
770 quiescence escalate to the 2020–2021 surge of Sít’Kusá, southeast Alaska. *Journal of Glaciology*, 1–12
- 771 Lovell H and Fleming EJ (2023) Structural evolution during a surge in the Paulabreen glacier system, Svalbard.
772 *Journal of Glaciology*, **69**(273), 141–152
- 773 Luthcke S and 7 others (2021) Icesat-2 pointing calibration and geolocation performance. *Earth and Space Science*,
774 **8**(3), e2020EA001494
- 775 Magruder L, Neumann T and Kurtz N (2021) ICESat-2 Early Mission Synopsis and Observatory Performance. *Earth*
776 *and Space Science*, **8**(5), e2020EA001555

- 777 Main B and 6 others (2024) Topographic and hydrological controls on partial and full surges of Little Kluane Glacier,
778 Yukon. *Journal of Glaciology*, 1–37
- 779 Markus T and 24 others (2017) The Ice, Cloud, and land Elevation Satellite-2 (ICESat-2): Science requirements,
780 concept, and implementation. *Remote Sensing of Environment*, **190**, 260–273
- 781 Martino AJ, Neumann TA, Kurtz NT and McLennan D (2019) Icesat-2 mission overview and early performance. In
782 *Sensors, Systems, and Next-generation Satellites XXIII*, volume 11151, 68–77, SPIE
- 783 Meier M and Post A (1969) What are glacier surges? *Canadian Journal of Earth Sciences*, **6**(4), 807–817
- 784 Murray T, Strozzi T, Luckman A, Jiskoot H and Christakos P (2003) Is there a single surge mechanism? Contrasts
785 in dynamics between glacier surges in Svalbard and other regions. *Journal of Geophysical Research: Solid Earth*,
786 **108**, B5
- 787 Neumann T and 8 others (2020a) ATLAS/ICESat-2 L2A Global Geolocated Photon Data, Version 5
- 788 Neumann T and 9 others (2020b) *ICESat-2 Algorithm Theoretical Basis Document for Global Geolocated Photons*,
789 *April 2020*. NASA ICESat-2 Project, 207p
- 790 Neumann T and 20 others (2019) The Ice, Cloud, and Land Elevation Satellite–2 mission: A global geolocated photon
791 product derived from the Advanced Topographic Laser Altimeter System. *Remote Sensing of Environment*, **233**,
792 111325
- 793 Nuth C and 9 others (2019) Dynamic vulnerability revealed in the collapse of an Arctic tidewater glacier. *Scientific*
794 *Reports*, **9**(1), 5541
- 795 Paul F and 8 others (2021) Three different glacier surges at a spot: what satellites observe and what not. *The*
796 *Cryosphere Discussions*, **2021**, 1–37
- 797 Post A (1972) Periodic surge origin of folded medial moraines on Bering Piedmont Glacier, Alaska. *Journal of*
798 *Glaciology*, **11**(62), 219–226
- 799 Roy DP and 33 others (2014) Landsat-8: Science and product vision for terrestrial global change research. *Remote*
800 *Sensing of Environment*, **145**, 154–172
- 801 Sevestre H, Benn DI, Hulton NR and Bælum K (2015) Thermal structure of Svalbard glaciers and implications for
802 thermal switch models of glacier surging. *Journal of Geophysical Research: Earth Surface*, **120**(10), 2220–2236
- 803 Shupe MD and 6 others (2011) Clouds at Arctic atmospheric observatories. Part I: Occurrence and macrophysical
804 properties. *Journal of Applied Meteorology and Climatology*, **50**(3), 626–644
- 805 Smith B and 13 others (2020) *ICESat-2 Algorithm Theoretical Basis Document for Land Ice Along-Track Height*
806 *Product, February 20, 2020*. NASA ICESat-2 Project, Greenbelt, Maryland, U.S.A., 107p
- 807 Strozzi T, Paul F, Wiesmann A, Schellenberger T and Käab A (2017) Circum-Arctic changes in the flow of glaciers
808 and ice caps from satellite SAR data between the 1990s and 2017. *Remote Sensing*, **9**(9), 947

- 809 Trantow T (2020) *Surging in the Bering-Bagley Glacier System, Alaska – Understanding Glacial Acceleration through*
810 *New Methods in Remote Sensing, Numerical Modeling and Model-Data Comparison*. Ph.D. thesis, University of
811 Colorado
- 812 Trantow T and Herzfeld U (2016) Spatiotemporal mapping of a large mountain glacier from CryoSat-2 altimeter
813 data: surface elevation and elevation change of Bering Glacier during surge (2011-2014). *International Journal of*
814 *Remote Sensing*, 0–28
- 815 Trantow T and Herzfeld UC (2018) Crevasses as indicators of surge dynamics in the Bering Bagley Glacier System,
816 Alaska: Numerical experiments and comparison to image data analysis. *Journal of Geophysical Research: Earth*
817 *Surface*
- 818 Trantow T and Herzfeld UC (2024) Evolution of a Surge Cycle of the Bering-Bagley Glacier System From Observations
819 and Numerical Modeling. *Journal of Geophysical Research: Earth Surface*, **129**(1), e2023JF007306
- 820 Truffer M and Echelmeyer KA (2003) Of isbrae and ice streams. *Annals of Glaciology*, **36**(1), 66–72
- 821 Truffer M and 11 others (2021) Glacier surges. In *Snow and Ice-related Hazards, Risks, and Disasters*, 417–466,
822 Elsevier
- 823 Vale AB, Arnold NS, Rees WG and Lea JM (2021) Remote detection of surge-related glacier terminus change across
824 High Mountain Asia. *Remote Sensing*, **13**(7), ISSN 2072-4292
- 825 Veci L, Prats-Iraola P, Scheiber R, Collard F, Fomferra N and Engdahl M (2014) The Sentinel-1 toolbox. In
826 *Proceedings of the IEEE International Geoscience and Remote Sensing Symposium (IGARSS)*, 1–3, IEEE
- 827 Willis MJ and 11 others (2018) Massive destabilization of an arctic ice cap. *Earth and Planetary Science Letters*,
828 **502**, 146–155
- 829 Wuite J, Libert L, Nagler T and Jóhannesson T (2022) Continuous monitoring of ice dynamics in Iceland with
830 Sentinel-1 satellite radar images. *Jökull*, **72**, 1–20
- 831 Yao X, Zhou S, Sun M, Duan H and Zhang Y (2023) Surging glaciers in High Mountain Asia between 1986 and 2021.
832 *Remote Sensing*, **15**(18), 4595
- 833 Zwally H and 15 others (2002) ICESat’s laser measurements of polar ice, atmosphere, ocean, and land. *Journal of*
834 *Geodynamics*, **34**(3-4), 405–445